

EVIDENCE FOR EXTENSIVE EXTENDED STAR FORMATION IN THE GALACTIC CENTER CLOUD SGR B2

ADAM GINSBURG^{1,2}

¹ Jansky fellow of the National Radio Astronomy Observatory, Socorro, NM 87801 USA

² European Southern Observatory, Karl-Schwarzschild-Straße 2, D-85748 Garching bei München, Germany

ABSTRACT

We report ALMA observations with resolution $\approx 0.5''$ at 3 mm of the extended Sgr B2 cloud. We detected 271 compact sources, the majority of which have extents smaller than 5000 AU. By ruling out alternative possibilities such as externally ionized globules, we conclude that these sources consist of a mix of HCH II regions and protostars, with most of the newly-detected sources being protostars. Based on their luminosities, most of these sources must have $M \gtrsim 8 M_{\odot}$. The spatial distribution of these sources, which is spread over a $\sim 12 \times 3$ pc region, demonstrates that Sgr B2 is experiencing an extended star formation event, not just an isolated ‘starburst’ within the protocluster regions Main (M), North (N), and South (S). Using this new sample, we examine star formation thresholds and surface density relations in Sgr B2. While all of the detected sources reside in regions of high column density ($N(\text{H}_2) \gtrsim 2 \times 10^{23} \text{ cm}^{-2}$), not all regions of high column density contain 3 mm sources. The observed threshold for star formation is substantially higher than that in solar vicinity clouds, implying either that high-mass star formation requires a higher column density or that the star formation threshold in the CMZ is higher than in nearby, low-mass clouds. The relation between the surface density of gas and stars has a slope similar to that observed in nearby clouds, but with a normalization at least an order of magnitude lower. We examine the spatial distribution of the new sources and determine that, out of the considered options of cloud-cloud collisions, expanding wind-driven bubbles, and pericenter triggering, no single model explains the observed distribution of present-day star formation, suggesting that the observed star formation is driven by several independent mechanisms working in conjunction. These observations constitute the largest known single, possibly coeval, sample of forming massive stars.

“extensive” will be removed from the title at a later date, but for now you must live with the excessive alliteration.

This version produced Thursday 20th July, 2017 at 17:41.

1. INTRODUCTION

The Central Molecular Zone (CMZ) of our Galaxy appears to be overall deficient in star formation relative to the gas mass it contains (Beuther et al. 2012; Immer et al. 2012; Longmore et al. 2013; Kauffmann et al. 2016a,b; Barnes et al. 2017). This deficiency suggests that star formation laws, i.e., the empirical relations between the star formation rate and gas column density, are not universal. The gas conditions in the Galactic center are different from those in nearby clouds, providing a long lever arm in a few parameters (e.g., pressure, temperature, velocity dispersion; Kruijssen & Longmore 2013; Ginsburg et al. 2016; Immer et al. 2016; Shetty et al. 2012; Henshaw et al. 2016) that facilitates measurements of the influence of environmental effects on star formation.

The CMZ dust ridge contains most of the dense molecular material in the Galactic center (Lis et al. 1999; Bally et al. 2010; Molinari et al. 2011). The observed star formation deficiency comes from comparing the quantity of dense gas to star formation tracers such as water masers (Longmore et al. 2013), infrared source counts (Yusef-Zadeh et al. 2009), or integrated infrared luminosity (Barnes et al. 2017).

Recent searches for ongoing star formation using high-resolution millimeter observations of selected clouds in the CMZ have revealed very star-forming cores (Johnston et al. 2014; Rathborne et al. 2014, 2015; Kauffmann et al. 2016a,b). As summarized by Barnes et al. (2017), most of the dust ridge clouds contain $< 1000 M_{\odot}$ of stars, or $\sim 2\%$ of their mass in stars. The Sgr B2 N (North), M (Main), and S (South) protoclusters (Schmiedeke et al. 2016, Figure 1) are exceptional in that they are actively forming star clusters and contain high-mass protostars and many compact H II regions (e.g., Higuchi et al. 2015; Gaume et al. 1995); despite the active star formation, the overall cloud appears to be as inefficient as the other dust ridge clouds (Barnes et al. 2017). Besides Sgr B2, a few of the dust ridge regions are forming stars at a much lower level, including the 20 km s^{-1} and 50 km s^{-1} clouds (Lu et al. 2015; ?, ?, Sgr C (Kendrew et al. 2013), and Clouds C, D, and E (Ginsburg et al. 2015; Barnes et al. 2017, Walker et al, in prep;). These regions contain only a small number of high-mass cores, protostars, and small H II regions.

Most observations of the Sgr B2 cloud focus on the “hot cores” Sgr B2 N and M, which are high-mass protoclusters. The extended cloud has been the subject of some studies in gas tracers, but it has never been observed at high ($\lesssim 10''$) resolution in the far infrared or millimeter regime. Radio observations at $\nu < 25 \text{ GHz}$ have revealed extended NH₃ and several masers (Martín-

Pintado et al. 1999; McGrath et al. 2004; Caswell et al. 2010), but these tracers only detect a subset of star-forming sources. Martín-Pintado et al. (1999) suggested the presence of ongoing star formation in the broader Sgr B2 cloud based on the detection of three NH₃ 4-4 ‘hot cores’ south of Sgr B2 S. Despite this suggestion, and the high density of gas throughout the broader Sgr B2 cloud, an extended star formation event has not been verified.

We report the first observations of extended, ongoing star formation in the Sgr B2 cloud. We observed a $\sim 15 \times 15 \text{ pc}$ section of the Sgr B2 cloud and identified star formation along the entire molecular dust ridge known as Sgr B2 Deep South (DS, also known as the ‘Southern Complex’ Jones et al. 2012; Schmiedeke et al. 2016). These observations allow us to perform one of the best star-counting based determinations of the star formation rate within the dense molecular gas of the CMZ.

We adopt a distance to Sgr B2 $D_{\text{SgrB2}} = 8.4 \text{ kpc}$, which is consistent with Sgr B2 being located in the CMZ dust ridge. While Reid et al. (2009) measure a closer distance of $7.9 \pm 0.8 \text{ kpc}$, we use a value closer to the IAU-recommended Galactic Center distance of 8.5 kpc, accounting for the distance difference of $\approx 100 \text{ pc}$ measured by Reid et al. (2009)¹. Choosing the closer distance would result in masses and luminosities smaller by 12%, which would not affect any of the conclusions of this paper.

We describe the observations in Section 2. In this paper, we focus on the continuum sources, which we identify in Section 3.1. We classify the sources in Section 3.3. **TODO: complete this ‘overview of the paper’ once all sections have been included.**

2. OBSERVATION AND DATA REDUCTION

2.1. ALMA data

Data were acquired as part of ALMA project 2013.1.00269.S (see Table 1). Observations were taken in ALMA Band 3 with the 12m Total Power array, the ALMA 7m array, and in two configurations with the ALMA 12m array. The setup included the maximum allowed number of channels, 30720, across 4 spectral windows in a single polarization; the single-polarization mode was adopted to support moderate spectral resolution ($\sim 0.8 \text{ km s}^{-1}$, 244 kHz channels) across the broad bandwidth. The basebands were centered at 89.48, 91.28, 101.37, and 103.23 GHz with bandwidth 1.875 GHz (total 7.5 GHz). The off position used to cali-

¹Reid et al. (2014) also conclude that the distance to the Galactic center is 8.34 kpc, suggesting that the direct parallax measurement to Sgr B2 is underestimated.

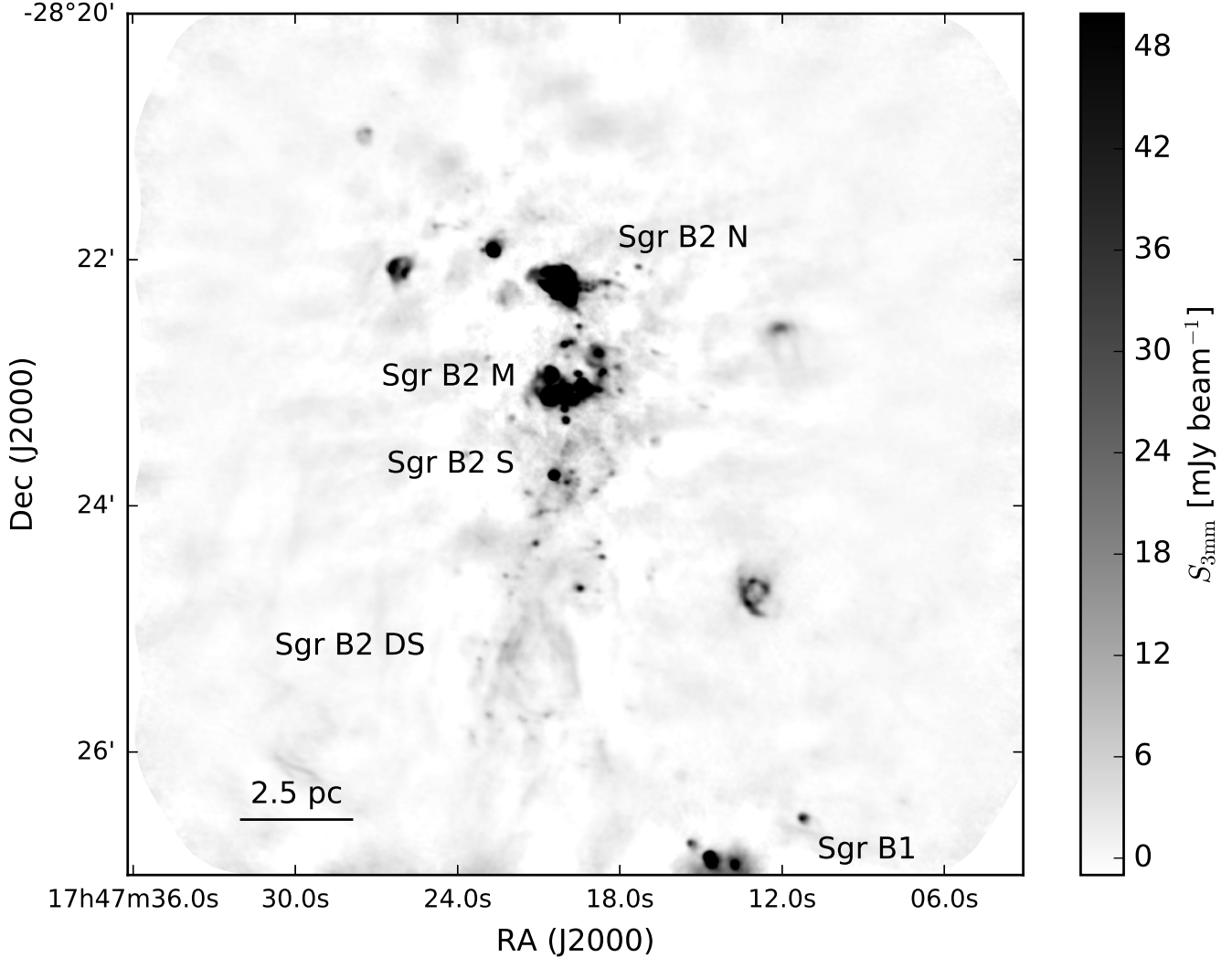


Figure 1. An overview of the Sgr B2 region, with the most prominent regions labeled. The image shows the ALMA 3 mm observations imaged with $1.5''$ resolution to emphasize the larger scale emission features. For a cartoon version of this figure, see Schmiedeke et al. (2016) Figure 1.

breathe the system temperature for the Total Power (TP) observations was at J2000 17:52:06.461 -28:30:32.095.

The ALMA QA2 calibrated measurement sets were combined to make a single high-resolution, high-dynamic range data set. We imaged the continuum jointly across all four basebands (without excluding any spectral line regions), and found that the central regions surrounding Sgr B2 M were severely affected by artifacts that could not be cleaned out. We therefore ran 3 iterations of phase-only self-calibration and two iterations of amplitude + phase self-calibration, the latter using multi-scale multi-frequency synthesis with two Taylor terms (Rau & Cornwell 2011), to yield a substantially improved image (see Appendix B). The total dynamic range, measured as the peak brightness in Sgr B2 to the RMS noise in a signal-free region of the combined

7m+12m image, is 18000 (noise ~ 0.09 mJy/beam, 0.05 K), while the dynamic range within one primary beam ($\sim 0.5'$) of Sgr B2M is only 5300 (noise ~ 0.3 mJy/beam, 0.16 K). Because of the dynamic range limitations and an empirical determination that clean did not converge if allowed to go too deep, we cleaned to a threshold of 0.1 mJy/beam over all pixels with $S_\nu > 2.5$ mJy / beam as determined from a previous iteration of `clean`. The final image used for most of the analysis in this paper was imaged with Briggs robust parameter 0.5, achieving a beam size $0.54'' \times 0.46''$.

We also produced full spectral data cubes. These were lightly cleaned with a maximum of 2000 iterations of cleaning to a threshold of 100 mJy/beam. The noise is typically ≈ 9 mJy beam^{-1} (6 K) per 0.8 km s^{-1} channel in the robust 0.5 cubes. No self-calibration was

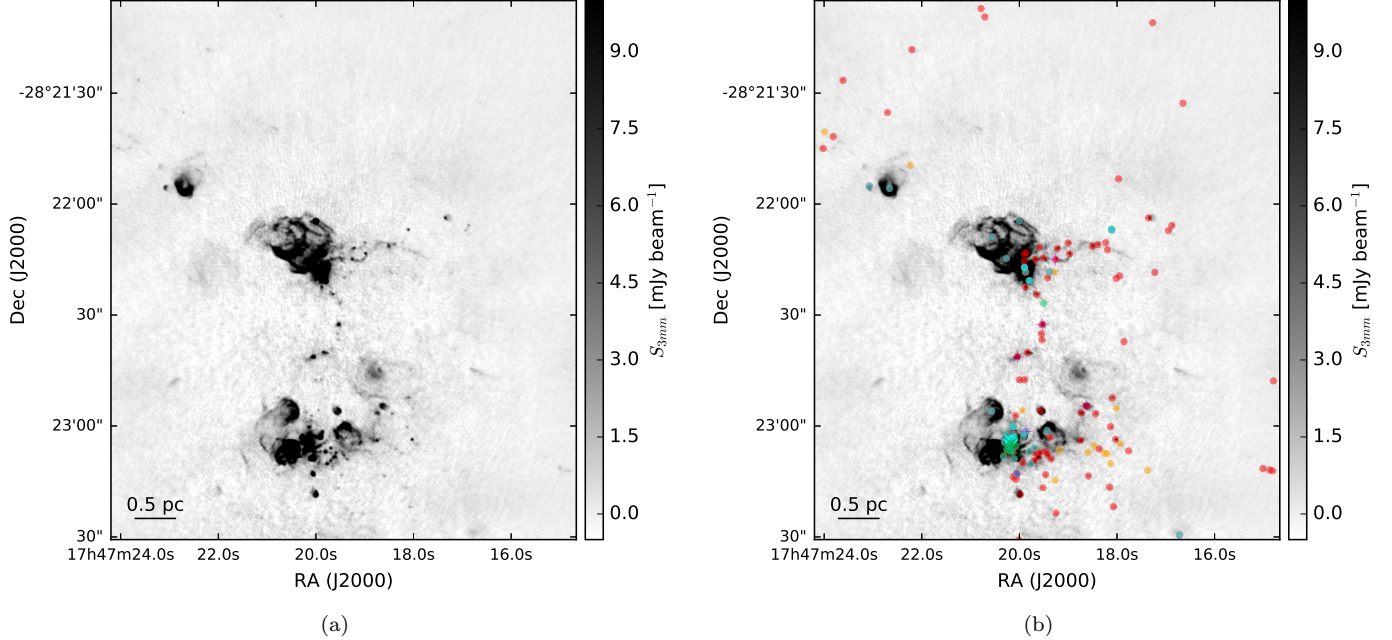


Figure 2. Images of the ALMA 3 mm continuum in the Sgr B2 M and N region. The right figure additionally includes markers at the position of each identified continuum pointlike source: red dots are ‘conservative’, high-confidence sources, orange dots are ‘optimistic’, low-confidence sources, cyan are H II regions, magenta +’s are masers, and green X’s are X-ray sources. The massive protocluster Sgr B2 M is the collection of H II regions and compact sources in the lower half of the image. The other massive protocluster, Sgr B2 N, is in the center. Imaging artifacts (sidelobes) are evident at the 1-2 mJy bm^{-1} level. The crowded parts of the images are shown with inset zoom-in panels in Figure 3.

Table 1. Observation Summary

Date	Array	Observation Duration seconds	Longest Baseline Length meters	# of antennae
01-Jul-2014	7m	4045	49	10
02-Jul-2014	7m	4043	49	10
03-Jul-2014	7m	7345	48	8
06-Dec-2014	12m	6849	349	34
01-Apr-2015	12m	3464	328	28
02-Apr-2015	12m	3517	328	39
01-Jul-2015	12m	3517	1574	43
02-Jul-2015	12m	10598	1574	42
25-Jan-2015	12m TP	6924	89	3
01-Apr-2015	12m TP	1986	67	2
11-Apr-2015	12m TP	6920	89	3
12-Apr-2015	12m TP	10441	89	3
25-Apr-2015	12m TP	13928	89	3
26-Apr-2015	12m TP	22562	186	3
18-May-2015	12m TP	8342	89	3

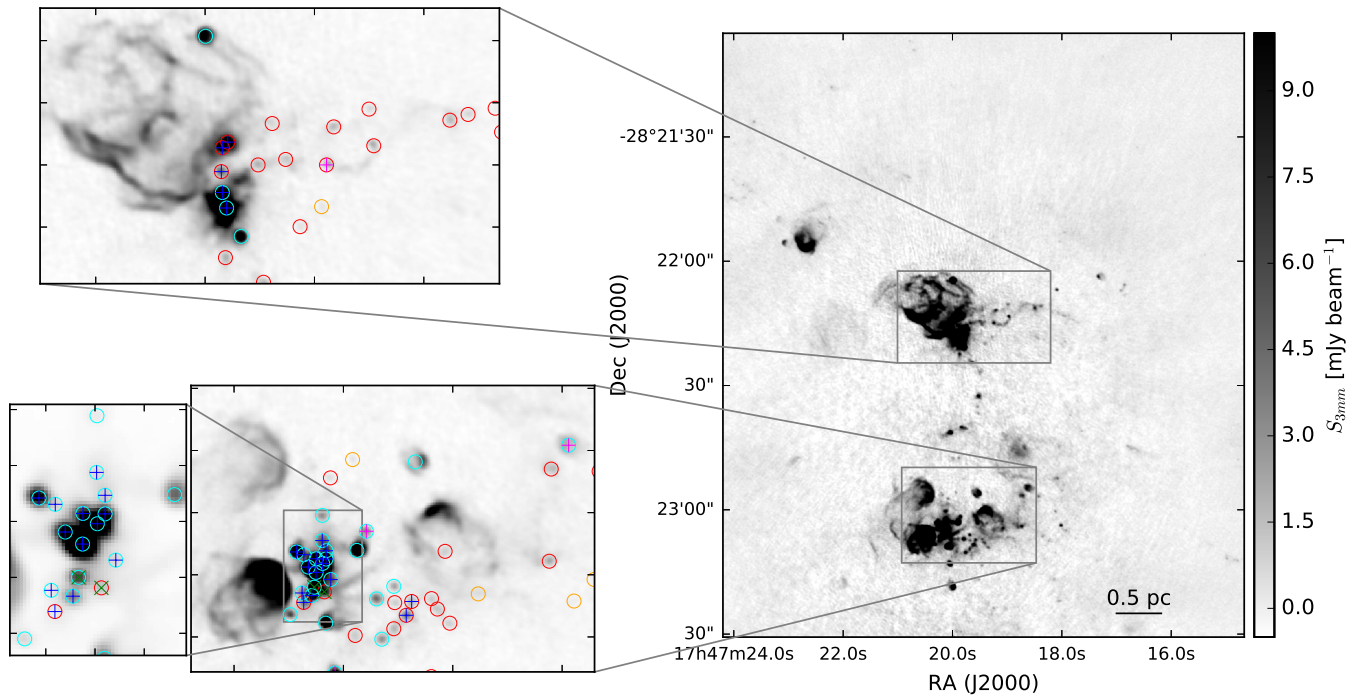


Figure 3. A close-in look at the Sgr B2 M and N region. Multiple insets show identified sources in some of the richer sub-regions. The points are colored as in Figure 2. The background image is the ALMA 3 mm continuum. See also Figure 22.

applied, both because the dynamic range limitations were less significant and because the image cubes are computationally expensive to process. Before continuum subtraction, dynamic range related artifacts similar to those in the continuum images were present, but these structures are identical across frequencies, and were therefore removable in the image domain. We use median-subtracted cubes (i.e., spectral cubes with the median along each spectrum treated as continuum and subtracted) for our analysis of the lines, noting that the only location in which an error $> 5\%$ on the median-estimated continuum is expected is the Sgr B2 North core (Sanchez-Monge et al. 2017, Sanchez-Monge et al. 2017, submitted). While many lines were included in the spectral setup, only HC₃N J=10-9 is discussed here; of the included lines, it is the brightest and most widely detected. This line has a critical density $n_{cr} \equiv A_{ij}/C_{ij} \approx 5 \times 10^5 \text{ cm}^{-3}$ (Green & Chapman 1978), so it would traditionally be considered a high-density gas tracer.

The processed data are available from http://apps.canfar.net/storage/list/SgrB2_ALMA_3mm in the form of four $\sim 225 \text{ GB}$ data cubes. Additional data sets will be made available via dataverse or some other service prior to submission.

2.2. Other data - Column Density Maps

We use archival data to create column density maps at a coarser resolution than the ALMA data, since the ALMA data are not sensitive enough to make direct column density measurements. We use Herschel Hi-Gal data (Molinari et al. 2010) to perform SED fits to each pixel (Battersby et al, in prep). These fits were performed at $25''$ resolution, using the 70, 160, 250, and $350 \mu\text{m}$ data and excluding the $500 \mu\text{m}$ channel. The estimated uncertainty is $\sim 25\%$, with an upper limit on the systematic uncertainty of a factor of two (Batterby et al, in prep). To obtain column density maps with greater resolution, we combine the Herschel data with SHARC $450 \mu\text{m}$ and SCUBA $350 \mu\text{m}$ images.

The CSO SHARC data were reported in Bally et al. (2010) and have a nominal resolution of $9''$ at $350 \mu\text{m}$, however, at this resolution, the SHARC data display a much higher surface brightness than the Herschel data on the same angular scale. An assumed resolution of $11.5''$ gives a better surface brightness match and is consistent with the measured scale of Sgr B2 N in the image. This calibration difference is likely to have been a combination of blurring by pointing errors, surface imperfections, and the gridding process, which all increase the effective beam size, and flux calibration errors. In any case, the Herschel data provide the most trustworthy

absolute calibration scale, since they were taken from space and calibrated to an absolute scale using Planck data (Bendo et al. 2013; Bertincourt et al. 2016).

The JCMT SCUBA $450 \mu\text{m}$ data were reported in Pierce-Price et al. (2000) and Di Francesco et al. (2008) with a resolution of $8''$. We found that the SCUBA data had a flux scale significantly discrepant from the Herschel-SPIRE $500 \mu\text{m}$ data on $30\text{-}90''$ scales, even accounting for the central wavelength difference. We had to scale the SCUBA data up by a factor ≈ 3 to make the data agree with the Herschel-SPIRE images on these scales. While such a large flux calibration error seems implausible, it is plausible if the beam size of the ground-based data is larger than expected. To assess this possibility, we fit 2D Gaussians to several sources in the SCUBA CMZ maps, measuring a FWHM toward Sgr B2 N of approximately $14''$, which means the beam area is $\approx 3\times$ larger in area than the theoretical size. Among several other sources fit in the SCUBA map, the smallest FWHM measured was $\approx 10.5''$. Between the larger beam area, flux calibration errors (quoted at 20% in Pierce-Price et al. 2000), and the dust emissivity correction (35-50% for $\beta = 3 - 4$), this large flux scaling factor is plausible. This large correction factor is consistent with the large error beam found by Di Francesco et al. (2008), with effective FWHM $\approx 17.3''$, since they used additional smoothing when creating their maps. As with the SHARC data above, we trust the space-based calibration over the ground-based.

To obtain higher resolution column density maps, we used the combined Herschel-SPIRE+SHARC and Herschel-SPIRE+SCUBA maps. We created several column density maps, some assuming arbitrary constant temperatures equal to the minimum and maximum expected dust temperatures (20 and 50 K), and another using the temperature measured with Herschel interpolated onto the higher-resolution SCUBA and SHARC grids. Because of the interpolation and fixed temperature assumptions, the column maps are not very accurate and should not be used for systematic statistical analysis of the column density distribution (i.e., PDF shape analysis) without careful attention to the large implied uncertainties. However, these higher-resolution data are used in this paper to provide the best estimates of the local column density around our sample of compact millimeter continuum sources. The data combination is discussed in more detail in Appendix A.

3. ANALYSIS

3.1. Continuum Source Identification

We selected compact continuum sources by eye, scanning across images with different weighting schemes (dif-

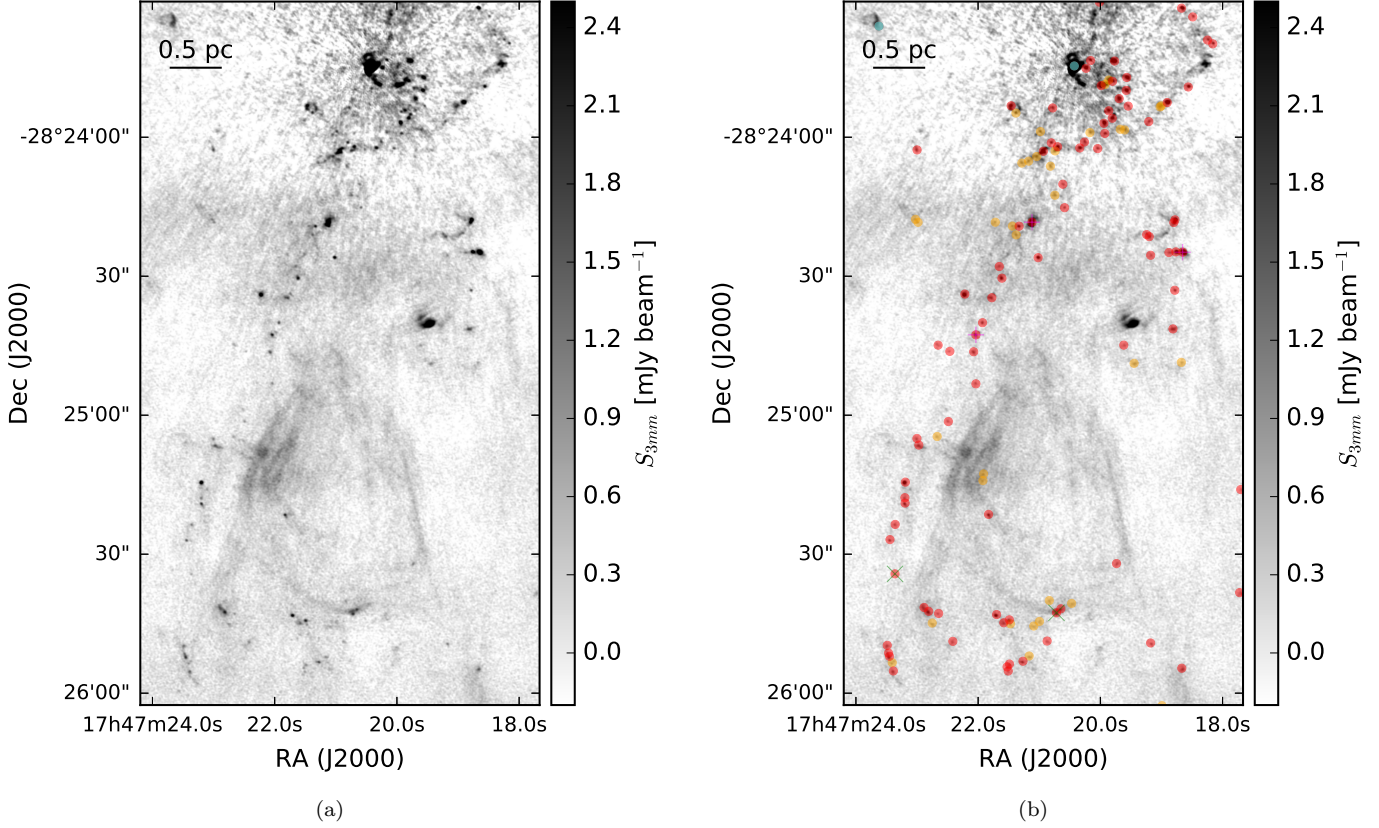


Figure 4. Images of the ALMA 3 mm continuum in the Sgr B2 Deep South (DS) region. The right figure additionally includes markers at the position of each identified continuum pointlike source: red dots are ‘conservative’, high-confidence sources, orange dots are ‘optimistic’, low-confidence sources, cyan are H II regions, magenta +’s are masers, and green X’s are X-ray sources. The H II region Sgr B2 S is the bright source at the top of the image; imaging artifacts can be seen surrounding it. The largest angular scales are noisier than the small scales; the $\sim 20''$ -wide east-west ridge at around $-28:24:30$ is likely to be an imaging artifact. By contrast, the diffuse components in the southern half of the image are likely to be real. The crowded parts of the images are shown with inset zoom-in panels in Figure 5.

ferent robust parameters). An automated selection is not viable across the majority of the observed field for several reasons:

1. There are many extended H II regions that dominate the overall map emission. These are clumpy and have local peaks that would dominate the identified source population using most source-finding algorithms.
2. There are substantial imaging artifacts produced by the extremely bright emission sources in Sgr B2 M ($S_{3\text{mm},\text{max}} \approx 1.6$ Jy) and Sgr B2 N ($S_{3\text{mm},\text{max}} \approx 0.3$ Jy) that make automated source identification particularly challenging in the most source-dense regions. These are ‘side-lobes’ from the bright sources that cannot be entirely removed.
3. Resolved-out emission has left multi-scale artifacts throughout the images. While these can be filtered

out to a limited degree by excluding large angular scales (short baselines), there remain small-scale ripples, and the noise increases when baselines are excluded.

All of these features are evident in Figures 2 and 4.

Because the noise varies significantly across the map (it is higher near Sgr B2 M), and because there is extended emission, a uniform selection criterion is not possible. We therefore include two levels of source identification, ‘high confidence’ sources, which are selected conservatively in regions of low-background, and ‘low-confidence’ sources that are somewhat lower signal-to-noise and are often in regions with higher background (labeled ‘conservative’ and ‘optimistic’, respectively, in Figure 6 and 7); the difference between the criteria is subjective. We measure the local noise for each source by taking the median absolute deviation in an annulus 0.5 to $1.5''$ around the source center; these noise measurements are reported in Table 3.

Outside of the dense clusters, every locally 5σ peak was visually inspected. Peaks that were part of extended structures but not significantly different from them (e.g., a 5σ peak sitting on a 4σ extended structure) were excluded. We excluded sources with extents $r > 1''$, i.e., extended H II regions.

Our selection criteria result in a reliable but potentially incomplete catalog; because we did not employ an automated source identification algorithm, we cannot readily quantify our completeness. The regions most likely to be incomplete near our noise threshold are Sgr B2 M and N. In these regions, dynamic range limitations increase the background noise and make fainter sources difficult to detect, as described in Section 2. Additionally, they both contain extended structures, including H II regions and dust filaments, which likely obscure compact sources.

For a subset of the sources, primarily the brightest, we measured the spectral index α based on CASA `tclean`'s 2-term Taylor expansion model of the data (parameters `deconvolver='mtmfs'` and `nterms=2`). This measurement is over a narrow frequency range (≈ 90 – 100 GHz). `tclean` produces α and $\sigma(\alpha)$ (error on α) maps, and we used the α value at the position of peak intensity for each source. We include in the analysis only those sources with $|\alpha| > 5\sigma(\alpha)$ or $\sigma(\alpha) < 0.1$; the latter include sources with $\alpha \sim 0$ measured at relatively high precision. 62 sources met these criteria. Several of the brightest sources did not have significant measurements of α because they are in the immediate neighborhood of Sgr B2 M or N and therefore have significantly higher background and noise, preventing a clear measurement. To check the calibration of the spectral index measurement, we imaged one of our calibrators, J1752-2956, and obtained a spectral index $\alpha = -0.62 \pm 0.14$, consistent with the expected $\alpha \approx -0.7$ for an optically thin synchrotron source (e.g., Condon & Ransom 2007). We also note that the *relative* spectral index measurements in our catalog should be accurate, since all sources come from the same map with identical calibration.

We detected 271 compact continuum sources, and they are listed in Table 3. Their flux distribution is shown in Figure 6. The distribution of their measured spectral indices α is shown in Figure 7. Generally, spectral indices $\alpha < 0$ indicate nonthermal (e.g., synchrotron) emission, $-0.1 < \alpha < 2$ may correspond to free-free sources of various optical depths, $\alpha = 2$ for any optically thick thermal source, and $\alpha > 2$ usually indicates optically thin dust emission. These indices will be discussed further in the next Section.

3.2. Catalog Cross-Matching

We cross-matched our source catalog with catalogs of NH₃ sources, H II regions, X-ray sources, Spitzer sources, and methanol and water masers. Associations with these types of sources can be used to classify the sources.

We classified sources as H II regions if there is a corresponding 0.7 or 1.3 cm source from one of the previous VLA surveys (Gaume et al. 1995; Mehringer et al. 1995; De Pree et al. 1996, 2015) within one ALMA beam ($0.5''$). 31 of our sources are classified as H II regions; these all have $S_{3\text{mm}} > 9$ mJy. The majority of these are unresolved, but we have included H II regions with radii up to $\approx 1''$ in our catalog. Optically thick H II regions (like any blackbody) have a spectral index $\alpha = 2$. Optically thin H II regions have a nearly flat spectral index, $\alpha = -0.1$ (Condon & Ransom 2007). The observed sources with H II region counterparts have spectral indices consistent with the theoretical expectation for optically thin H II regions in Figure 7. The existing VLA data do not cover the entire area of our observations, so we only have a lower limit on the number of H II regions in our sample; the sources in Sgr B2 DS have not yet been observed in the radio at high resolution. Sources matched with H II regions evidently contain high-mass (most likely $M \gtrsim 20 M_\odot$, see Section 3.3.3 below) young stars.

Martín-Pintado et al. (1999) observed part of Sgr B2 DS and M in NH₃ with the VLA. They identified three “hot cores” based on NH₃ 4-4 detections. Only their first source HC1 has an associated 3 mm continuum source, suggesting that HC2 and HC3 are not genuine hot cores but are some other variant of locally heated (perhaps shock-heated) gas. However, the association between HC1 and our source 43 suggests that it is a young stellar object with a massive envelope. Of the 6 NH₃ 3-3 maser sources identified by Martín-Pintado et al. (1999), three are in regions with high 3 mm source density but lack a clear one-to-one source association, one is coincident with an H II region not in our catalog, and two have no obvious associations; the NH₃ 3-3 masers therefore appear not to be unambiguous tracers of star formation in this environment, consistent with the conclusions of Mills et al. (2015).

Class II methanol masers are exclusively associated with sites of high-mass star formation. The Caswell et al. (2010) Methanol Multibeam (MMB) Survey identified 11 sources in our observed field of view (their survey covers our entire observed area), of which 10 have a clear match to within $1''$ of a source in our catalog (the MMB catalog sources have a positional accuracy of $\approx 0.4''$, but masers may have an extent up to $1''$). These sources are clearly identified as high-mass protostars. The single maser that does not have an associated

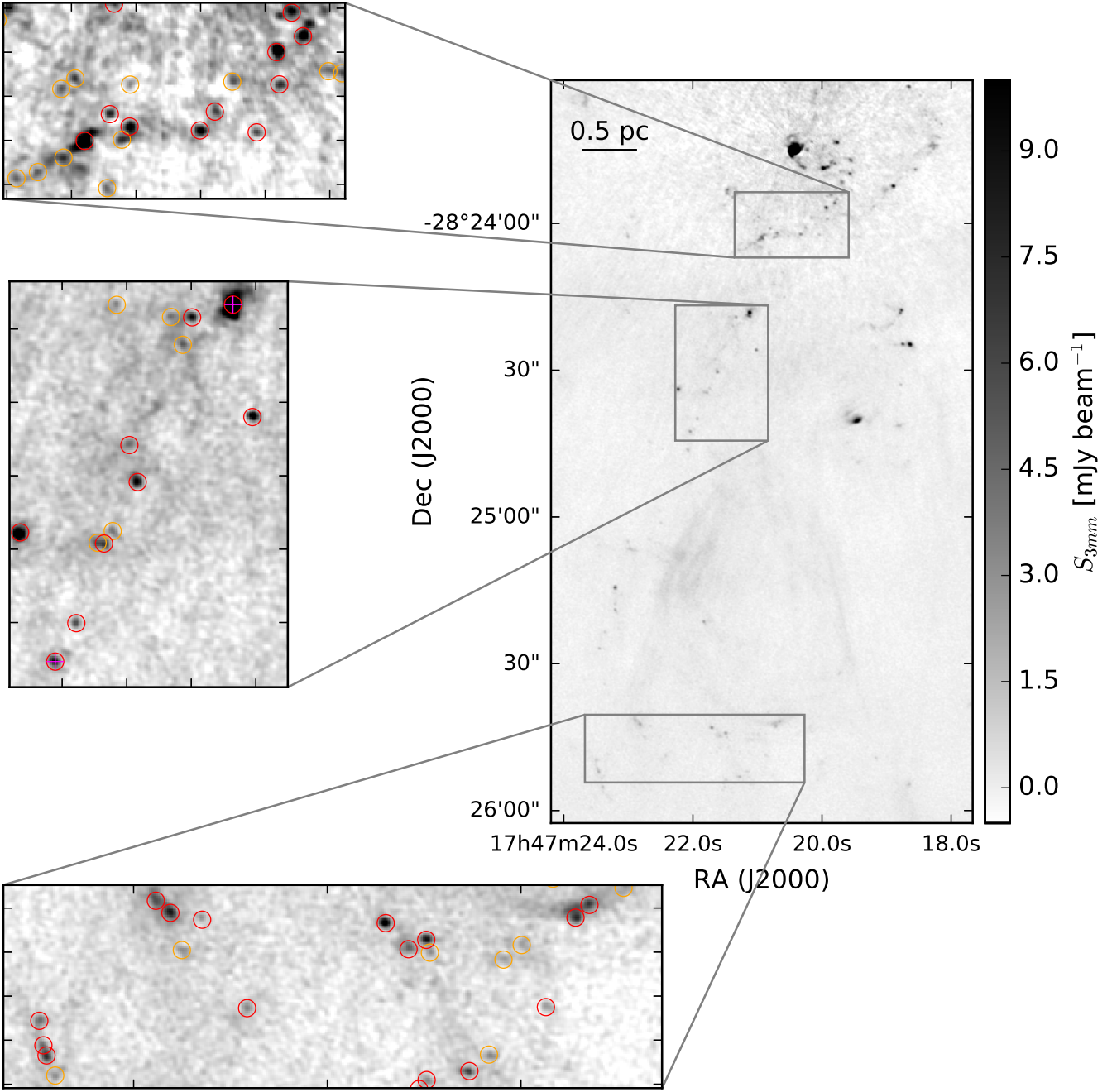


Figure 5. A close-in look at the Sgr B2 DS region. Multiple insets show identified sources in some of the richer sub-regions. The points are colored as in Figure 2. The background image is the ALMA 3 mm continuum.

millimeter source is $5''$ west of Sgr B2 S and resides near some very faint and diffuse 3 mm emission; it is unclear why the 3 mm is so weak here, but it hints that there are MYSOs with 3 mm emission below our detection limit.

Water masers are generally associated with forming young stars. We also matched our catalog with the McGrath et al. (2004) water maser catalog, finding that 23 of our sources have a water maser within $1''$. Again, these sources are likely to contain protostars, but not

necessarily HMYSOs based on their H_2O maser detections alone.

Some young stars exhibit X-ray emission, including some MYSOs (e.g., Townsley et al. 2014), so we searched for X-ray emission from our sources. 3 of the sources have X-ray counterparts in the Muno et al. (2009) Chandra point source catalog within $1''$. The Muno et al. (2009) catalog covers our entire observed area. The X-

ray associated sources most likely either contain protostars or young stars.

We searched the Yusef-Zadeh et al. (2009) catalogs of $4.5\text{ }\mu\text{m}$ excess sources and YSO candidates and found only one source association, though there are 5 and 14, respectively, of these sources in our field of view. Two of the $4.5\text{ }\mu\text{m}$ excess sources and one of the YSO candidates are associated with extended H II regions (which we do not catalog); the single association is of a $4.5\text{ }\mu\text{m}$ source with the central region of Sgr B2 M. By-eye comparison of the Spitzer maps and the ALMA images suggests that the lack of associations is at least in part because of the high extinction in the regions containing the 3 mm cores; there are overall fewer Spitzer sources in these parts of the maps.

Finally, we searched the Mehringer & Menten (1997) sample of 44 GHz CH₃OH masers and quasithermal sources for associations, finding no matches with any of our sources. This methanol line apparently does not trace star formation.

3.3. Source Classification

For the majority of the detected sources, we have only a continuum detection at 3 mm. In this section, we employ a variety of arguments to classify the sample of new sources. Most of our sources have no match in other catalogs (see Section 3.2), so we discuss what types of objects they could be given their 3 mm continuum detections. Plausible emission mechanisms include free-free and thermal dust emission, so we explore whether the sources could be different classes of free-free sources in subsections 3.3.1, 3.3.2, and 3.3.3. We conclude that they are primarily dusty sources in subsection 3.3.4.

We visually inspected the spectra extracted from the full line cubes, and no lines are detected peaking toward the majority of the sources (most sources have emission in some lines (e.g., HC₃N), but this emission is clearly extended and not associated with the compact source). Given the relatively poor line sensitivity (RMS $\approx 6\text{ K}$), the dearth of detections is not very surprising. We therefore cannot use spectral lines to classify most sources.

To aid in our classification, we note some properties of dust at 3 mm. The simplest assumption is that all sources we have detected that were not detected at longer wavelengths are pure dust emission sources at a constant temperature. At 8.4 kpc, a 1 mJy source corresponds to an optically thin gas mass² of $M(40\text{K}) = 18\text{ }M_{\odot}$ or $M(20\text{K}) = 38\text{ }M_{\odot}$ assuming a dust opacity index $\beta = 1.75$ ($\alpha = 3.75$ on the Rayleigh-Jeans tail) to extrapolate the Ossenkopf & Henning (1994, MRN

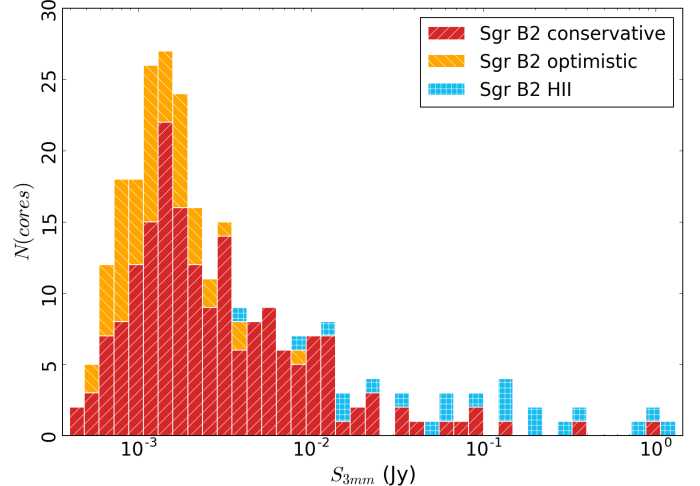


Figure 6. A histogram of the flux density (the peak intensity converted to flux density assuming the source is unresolved) of the observed sources. The histograms are stacked such that there are a total of 27 sources in the highest bin.

with thin ice mantles anchored at 1mm) opacity to $\kappa_{3.1\text{mm}} = 0.0018\text{ cm}^2\text{ g}^{-1}$ (per gram of gas). Our dust-only (i.e., excluding free-free emission) 5- σ sensitivity limit at 20 K therefore ranges from $M > 19\text{ }M_{\odot}$ (0.5 mJy) to $M > 94\text{ }M_{\odot}$ (2.5 mJy) across the map. If we were to assume that these are all cold, dusty sources, as is typically (and reasonably) assumed for local clouds, they would be extremely massive and dense, with the lowest measurable density being $n(20\text{K}) > 1 \times 10^8\text{ cm}^{-3}$ (corresponding to $19\text{ }M_{\odot}$ in an $r = 0.2'' = 1700\text{ AU}$ radius sphere). Such extreme objects are possible, but since we have detected > 100 of these sources, we evaluate other possibilities.

We start with a few alternatives we are able to rule out: externally ionized gas globules, internally ionized H II regions from an older generation of ‘interloper’ stars, and internally ionized H II regions from a newly-formed generation of massive stars. We then discuss why these sources are most likely embedded protostars.

3.3.1. Alternative 1: The sources are externally ionized gas blobs

One possibility is that these sources are not dust-dominated, nor pre- or protostellar, but are instead externally ionized, mostly neutral gas clumps embedded within diffuse H II regions. They would then be analogous to the heads of cometary clouds, externally ionized globules (“EGGs” Sahai et al. 2012a), or proplyds (externally ionized protoplanetary disks), and their observed emission would give little clue to their nature because the light source is extrinsic.

²We assume a gas-to-dust ratio of 100 throughout this work.

The majority of the detected sources have size < 4000 AU, i.e., they are unresolved. By contrast, the free-floating EGGs ('frEGGs') so far observed have sizes 10,000-20,000 AU (Sahai et al. 2012a,b), so they would be resolved in our observations. Toward the brightest frEGG in Cygnus X, Sahai et al. (2012b) measured a peak intensity $S_{8.5\text{GHz}} \approx 1.5$ mJy/beam in a $\approx 3''$ beam. Cygnus X is 6× closer than the Galactic center, so their beam size is the same physical scale as ours. If the free-free emission is thin ($\alpha = -0.1$), the brightness in our data would be $S_{95\text{GHz}} = (95/8.5)^{-0.1} S_{8.5\text{GHz}} = 0.79 S_{8.5\text{GHz}} \approx 1.2$ mJy/beam. These frEGGs would be detectable in our data. Comparison to radio observations at a similar resolution will be needed to rule out the externally ionized globule hypothesis for the resolved regions within our sample, but the unresolved sources are unlikely to be frEGGs.

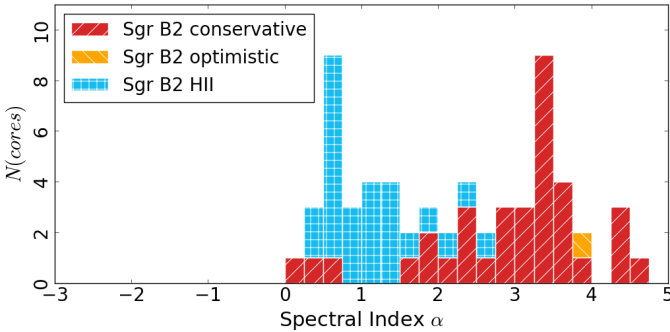


Figure 7. A histogram of the spectral index α for those sources with a statistically significant measurement. The H II regions cluster around $\alpha = 0$, as expected for optically thin free-free emission, while the unclassified sources cluster around $\alpha = 3.5$, which is consistent with dust emission.

If the detected sources were either EGGs or cometary clouds, we would expect them to be located within diffuse H II regions, since that is where all other sources of this type are seen, and since an external ionizing agent is needed to illuminate them. Many of the sources are near H II regions, as seen in Figure 8a, but not within them. The sources are nearly all associated with a ridge of molecular (HC₃N) emission (Figure 8b). If they are deeply embedded within the molecular material, they cannot be externally ionized. The fact that the ionized gas is brightest nearby, rather than directly on top of, the HC₃N suggests that the HC₃N traces a full molecular cloud rather than a thin PDR-like layer, which would be required if these sources are cometary clouds. The association with dense molecular gas implies that the sources are not externally ionized objects.

A final point against the externally ionized hypothesis is the observed spectral indices shown in Figure 7. We

measured spectral indices for 62 sources, of which 33 have $\alpha > 2$. These 33 sources are inconsistent with free-free emission and are at least reasonably consistent with dust emission.

3.3.2. Alternative 2: The sources are H II regions produced by interloper ionizing stars

If there is a large population of older (age 1-30 Myr) massive stars, they could ignite compact H II regions when they fly through molecular material. See 3.3.3 for calculations of stationary H II region properties. The main problem with this scenario is the spatial distribution of the observed sources. While most of the continuum sources are associated with dense gas and dust ridges, not all of the high-column molecular gas regions have such sources in them (i.e., Figure 8b, where molecular material is seen with no associated millimeter sources outside of the north/south HC₃N ridge). If there is a free-floating population of OB stars responsible for the 3 mm compact source population, if we assume the spatial distribution of the stars is uniform, the distribution of H II regions surrounding them should match that of the gas (since we are assuming the gas and stars are moving independently). Also, there is no such population of sources seen *outside* of the dense gas in the infrared, which again we should expect if there is a uniformly distributed massive stellar population. Finally, the spectral indices discussed above (Figure 7) suggest the previously-unidentified sources are dust emission sources, not free-free sources.

3.3.3. Alternative 3: The sources are H II regions produced by recently-formed OB stars

We know from previous observations (e.g., Mehringer et al. 1995; De Pree et al. 1996, 2015) that there is a substantial population of H II regions in the Sgr B2 clusters. The 31 sources associated with these previously-identified H II regions are among the brightest in our catalog. We address here whether the remaining sources, which are mostly fainter, could also be H II regions.

For an unresolved spherically symmetric H II region ($R = 4000$ AU), the expected flux density is $S_{95\text{GHz}} = 4.7$ mJy for a $Q_{lyc} = 10^{47}$ s⁻¹ source (assuming $T_e = 7000$ K), and that value scales linearly with Q_{lyc} as long as the source is optically thin. We rearrange Condon & Ransom (2007) equations 4.60 and 4.61 to get the expected flux density as a function of temperature, emission measure, and frequency:

$$S_\nu(Q_{lyc}) = 4.67 [1 - \exp(c_* T_* \nu_* EM_*)]$$

$$\nu_* = \left(\frac{\nu}{\text{GHz}}\right)^{-2.1}$$

$$T_* = \left(\frac{T_e}{10^4 \text{K}}\right)^{-1.35}$$

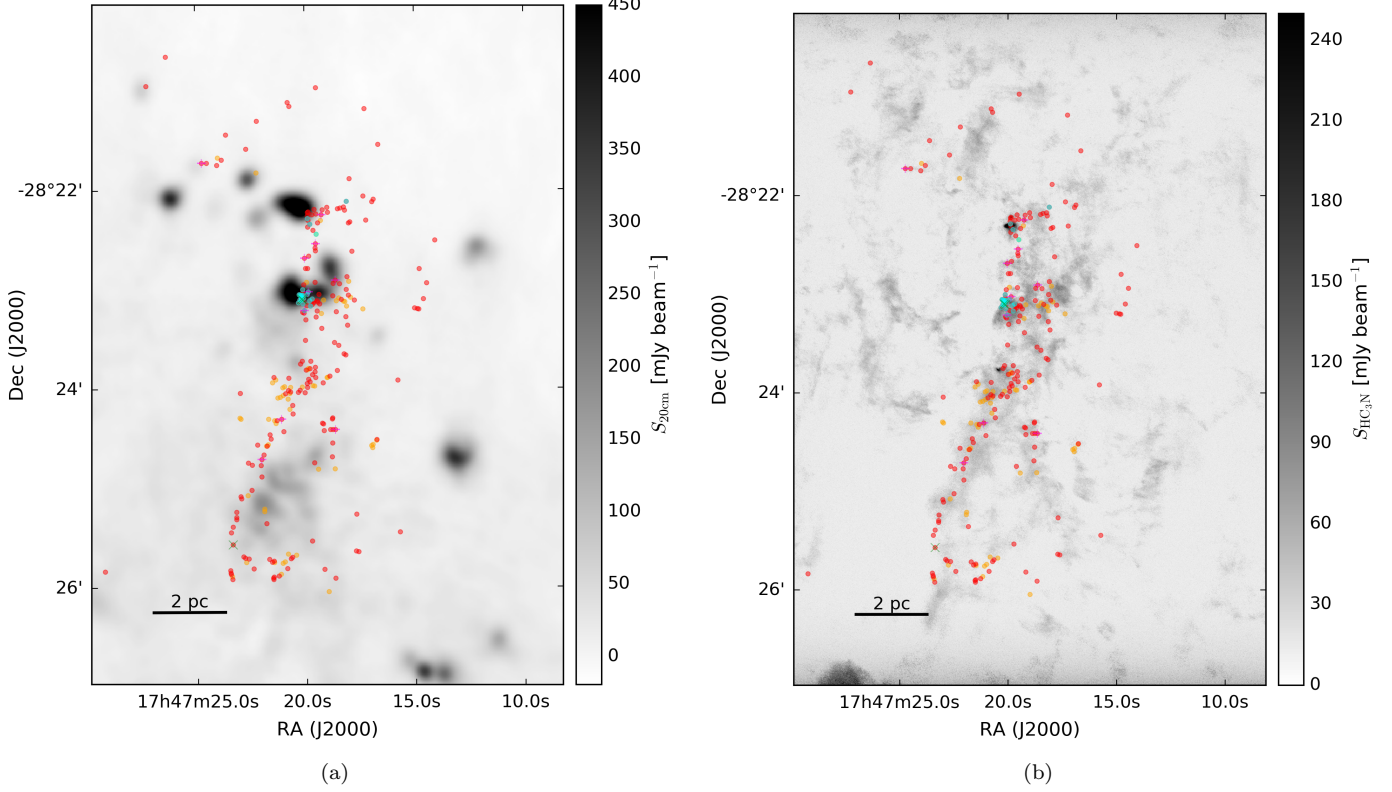


Figure 8. (left) The location of the detected continuum sources (red points) overlaid on a 20 cm continuum VLA map highlighting the diffuse free-free (or possibly synchrotron) emission in the region (Yusef-Zadeh et al. 2004). (right) Continuum sources overlaid on a map of the HC₃N J=10-9 peak intensity over the range [-200, 200] km s⁻¹. In both figures, red dots are ‘conservative’, high-confidence sources, orange dots are ‘optimistic’, low-confidence sources, cyan are H II regions, magenta +'s are masers, and green X’s are X-ray sources.

$$c_* = -3.28 \times 10^{-7}$$

$$EM_* = \frac{3Q_{lyc}}{4\pi R^2 \alpha_B} \quad (1)$$

where the case-B recombination coefficient $\alpha_B = 2 \times 10^{-13} \text{ cm}^3 \text{ s}^{-1}$, Q_{lyc} is the count rate of ionizing photons in s^{-1} , and R is the H II region radius. The constant c_* was computed by Mezger & Henderson (1967) as an approximation to the optical depth prefactor in the full radiative transfer equation and is never incorrect by more than $\approx 25\%$.

An extremely compact H II region, e.g., one with $R < 100 \text{ AU}$ and corresponding density $n > 10^6 \text{ cm}^{-3}$, would be optically thick and therefore fainter, $S_{95\text{GHz}}(R = 100\text{AU}, Q_{lyc} = 10^{47} \text{ s}^{-1}) = 3.4 \text{ mJy}$. Even the most luminous O-stars could produce H II regions as faint as 0.5 mJy if embedded in extremely high density gas; above $Q_{lyc} > 10^{47} \text{ s}^{-1}$, a 25 AU H II region would be $\sim 0.5 \text{ mJy}$.

Figure 9 shows the predicted brightness for various H II regions produced by OB stars and the density required for those H II regions to be the specified

size. There is a narrow range of late O/early B stars, $10^{46} < Q_{lyc} < 10^{47} \text{ s}^{-1}$, that could be embedded in compact H II regions of almost any size and produce the observed range of flux densities. In order for the detected sources to be O-star-driven H II regions, with $10^{47} < Q_{lyc} < 10^{50} \text{ s}^{-1}$, they must be optically thick and therefore extremely compact and dense. Anything fainter, later than $\sim B0$ ($Q_{lyc} < 10^{46} \text{ s}^{-1}$), would be incapable of producing the observed flux densities. Such bright stars would have to be embedded in dust that, at 40 K, would outshine the H II region. Figure 9b shows that the highest-luminosity stars would have to be embedded in $n > 10^8 \text{ cm}^{-3}$ gas to be small enough to produce an H II region with $S_{3\text{mm}} < 1 \text{ mJy}$, which means the dust - even if it were cold - would dominate the free-free emission. More likely, such sources would have much hotter dust and therefore would be much brighter (and more extended) than our observations allow.

The luminosity function of the observed sources is apparently steep (power law slope ≈ -2), assuming the flux density distribution (Figure 6) represents the luminosity distribution. The observed distribution cuts off near our sensitivity limit, which implies that the

steep spectrum should continue to lower luminosities, and therefore there are many more sources below our detection threshold than above. This argument is pure extrapolation, and therefore could easily be wrong, but if there is a large population of sources below < 0.5 mJy, they are certainly too faint to be H II regions (Figure 9a). Again, assuming the luminosity distribution is continuous, that implies that we have not detected H II regions.

This restrictive parameter space, combined with a steep luminosity function, is evidence against the population being dominated by H II regions. The spectral indices also support this conclusion, since some are steeper than $\alpha > 2$ and are therefore inconsistent with free-free emission.

3.3.4. Our hypothesis: The sources are (mostly) protostellar

After ruling out the other possibilities, we test and validate the hypothesis that most or all of the sources are protostellar in this section.

General calculations: As noted at the top of this section, a cold ‘ prestellar core’ at our detection limit would have $M(20\text{K}) \approx 20 M_{\odot}$ ($M(40\text{K}) \approx 10 M_{\odot}$). At these high densities ($n(20\text{K}) \gtrsim 10^8 \text{ cm}^{-3}$), it is unlikely any such cores are unbound. The high density required for our sources results in a very short free-fall timescale, $t_{ff} \lesssim 6000 \text{ yr}$, which suggests that the cores are unlikely to be prestellar cores and instead, even if their emission is dust-dominated, they contain protostars. Their emission is likely dust-dominated, but is probably warmer than the cloud average $T_D \sim 20 - 40 \text{ K}$.

If we assume higher dust temperatures, the inferred gas mass is lower, but an internal heating source - i.e., a protostar - is required. For example, if we assume $T_D = 80 \text{ K}$ ³, our detection limit is only $M(80\text{K}) = 4M_{\odot}$. Heating that much dust well above the cloud average requires a high-luminosity central heating source.

To constrain the required heating source, we examine the protostellar model grid of Robitaille (2017, specifically, the `spubhmi` and `spubsmi` models). The models that produce $S_{3\text{mm}} > 0.5 \text{ mJy}$ within a 5000 AU aperture uniformly have $L > 10^4 L_{\odot}$. Such luminosities imply either that an high-mass ($M \gtrsim 8 M_{\odot}$) star has already formed and is still surrounded by a massive envelope, or a high-mass YSO is present and accreting. The models of Zhang & Tan (2015), for example, generally

³At these dust temperatures, we should be concerned about the assumed opacity, since ices will begin to evaporate (e.g., Bergin et al. 1995), reducing the 3 mm opacity and correspondingly increasing the required mass required to produce the observed flux (Ossenkopf & Henning 1994).

only exhibit $L > 10^4 L_{\odot}$ once a star has reached $M \approx 10 M_{\odot}$ as it continues to accrete to a higher mass. Similarly, pre-main-sequence stellar evolution models (e.g., ?) only reach $L > 10^4 L_{\odot}$ for stars with final mass $M \gtrsim 8 M_{\odot}$. In the Robitaille (2017) model grid, all sources with $L > 10^5 L_{\odot}$ produce $S_{3\text{mm}} > 0.5 \text{ mJy}$, so our survey should be nearly complete to such sources, but in the range $10^4 L_{\odot} < L < 10^5 L_{\odot}$, a substantial fraction may be below our sensitivity limit.

Comparison to similar data: We compare our detected sample to that of the Herschel Orion Protostar Survey (HOPS; Furlan et al. 2016) in order to get a general empirical sense of what types of sources we have detected. We selected this survey for comparison because it is one of the largest protostellar core samples with well-characterized bolometric luminosities available. Figure 10 shows the HOPS source flux densities at $870\mu\text{m}$ (from LABOCA on the APEX telescope) scaled to $d = d_{SgrB2}$ and 3 mm assuming a dust opacity index $\beta = 1.5$, which is shallower than usually inferred, so the extrapolated fluxes may be slightly overestimated⁴. The $870\mu\text{m}$ data were acquired with a $\sim 20''$ FWHM beam, which translates to a resolution $\sim 1''$ at $d_{SgrB2} = 8.4 \text{ kpc}$ assuming $d_{Orion} = 415 \text{ pc}$, so our beam size is somewhat smaller than theirs.

The HOPS sources are all fainter than the Sgr B2 sources. The most luminous and brightest HOPS source, with $L_{tot} < 2000 L_{\odot}$, would only be 0.2 mJy in Sgr B2, or about a $2-\sigma$ source - below our detection threshold even in the noise-free regions of the map. We conclude that the Sgr B2 sources are much more luminous than any in the Orion sample, which is consistent with all of the sources in our sample being MYSOs.

This conclusion is supported by a more direct comparison with the Orion nebula as observed at 3 mm with MUSTANG (Dicker et al. 2009, Figure 11). Their data were taken at $9''$ FWHM resolution, corresponding to $0.48''$ at d_{SgrB2} . The peak flux density measured in that map is toward Source I, $S_{90GHz}(d_{SgrB2}) = 3.6 \text{ mJy}$. Source I⁵ would therefore be detected and would be somewhere in the middle of our sample. It resides on a background of extended emission, and the extended component would be readily detected (and resolved) in our data. Source I is the only known high-mass YSO in

⁴We err on the shallower side, implying that the extrapolated 3 mm fluxes are brighter, since this approach gives a more conservative view of the detectability of the Orion sources. In reality, such sources are likely even fainter than predicted here.

⁵This source includes Source I, BN, and a few other objects at this resolution, and at 3 mm Source I and BN are comparably bright (Plambeck et al. 2013). This source is not part of the HOPS sample.

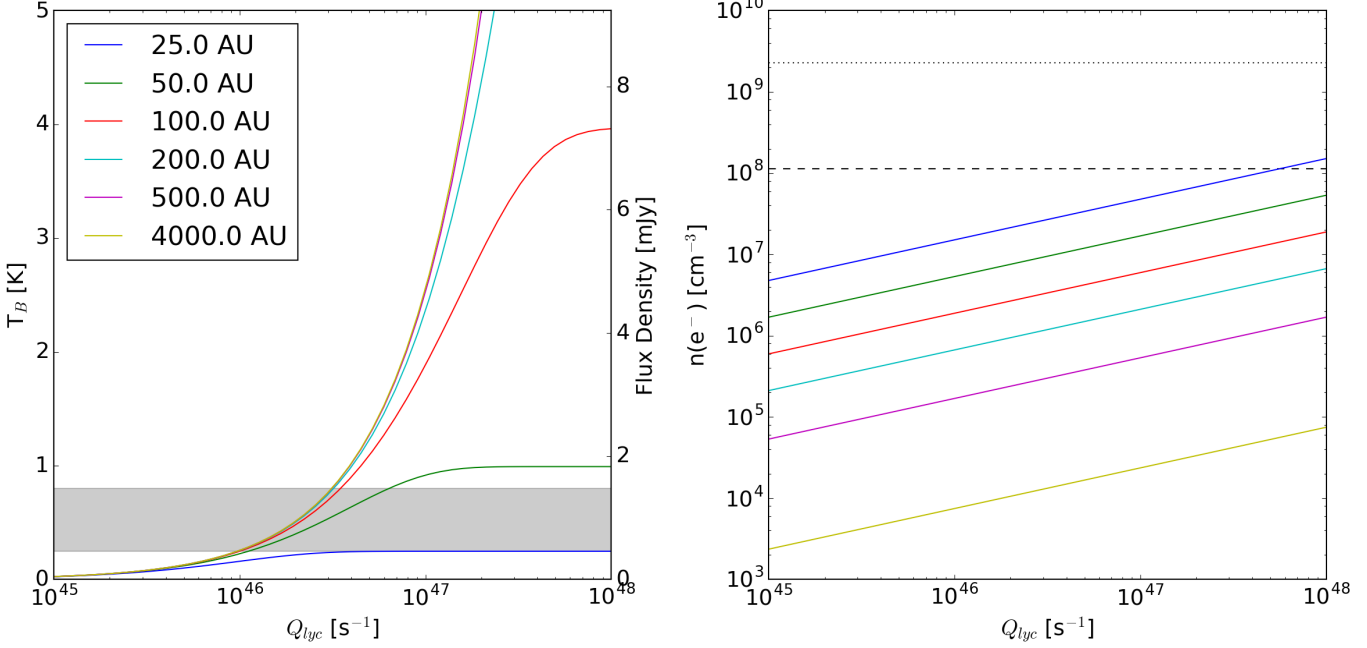


Figure 9. Simple models of spherical H II regions to illustrate the observable properties of such regions. The H II region size is shown by line color; the legend in the left plot applies to both figures. (left) The expected brightness temperature (left axis) and corresponding flux density at 95 GHz within a FWHM=0.5'' beam (right axis) as a function of the Lyman continuum luminosity for a variety of source radii. The grey filled region shows the range of our 5-sigma sensitivity limits, which vary with location from 0.25 to 0.8 K. (right) The density required to produce an H II region of that radius. The horizontal dashed line shows the density corresponding to an unresolved dust source ($r < 0.2'' = 1700$ AU) at the 5- σ detection limit (≈ 0.5 mJy, or about $10 M_\odot$ of dust, assuming $T = 40$ K). Above this line, dust emission would dominate over free-free emission. The dotted line shows the density required for dust emission to produce a 10 mJy source at $T = 40$ K. The density has been scaled by a factor of two, assuming $n_e = 2n(\text{H}_2)$. As seen in the left plot, for any moderate-sized H II region, $R > 100$ AU, a high-luminosity star ($Q_{lyc} > 10^{47} \text{ s}^{-1}$) would produce an H II region brighter than the majority of our sample, which includes only a few sources brighter than 10 mJy. The electron densities required to produce H II regions within our observed range ($1 < S_\nu < 10$ mJy) are fairly extreme, $n_e \gtrsim 10^6 \text{ cm}^{-3}$, for O-stars.

the Orion cloud, and it would be detectable in our survey while no other compact sources in the Orion cloud would be. This comparison supports the interpretation that most of the non-H II region sources are massive protostars.

While we have concluded that the sources are dusty, massive protostars, the spectral indices we measured are somewhat surprising. Typical dust clouds in the Galactic disk have dust opacity indices $\beta \sim 1.5 - 2$ (Schnee et al. 2010; Shirley et al. 2011; Sadavoy et al. 2016). Our spectral index measurements are lower than these, with only 3 sources (out of 62 with significant α measurements) having $\beta = \alpha - 2 > 1.5$ (at the 2 σ level, up to 11 sources are consistent with $\beta = 1.5$, but this is primarily because of their high measurement error). A shallower β implies free-free contamination, large dust grains, or optically thick surfaces are present within our sources. Since the above arguments suggest that the sources are high-mass protostars, the free-free contamination and optically thick inner region models are both plausible.

3.4. Source distribution functions and the star formation rate

In this section we examine the distribution of observed flux densities and the implied total stellar masses.

If we make the very simplistic, but justified (Section 3.3.4), assumption that the sources we detect all contain protostars with $L_{bol} \gtrsim 10^4 L_\odot$, and in turn make the related assumption that each source either currently contains or will form into an $M \gtrsim 8M_\odot$ star, we can infer the total (proto)stellar mass in the observed region.

We assume the stellar masses based on the arguments in Section 3.3.4: in order to be detected, the sources must either be active OB stars illuminating H II regions or cores, very compact cores with $M > 10 M_\odot$ of warm dust within $R < 4000$ AU, or at least moderately-massive protostars within warm envelopes. Note that the mass estimates in this section are for the resulting stars, not their envelopes. The cluster affiliation for each source is reported in Table 3.

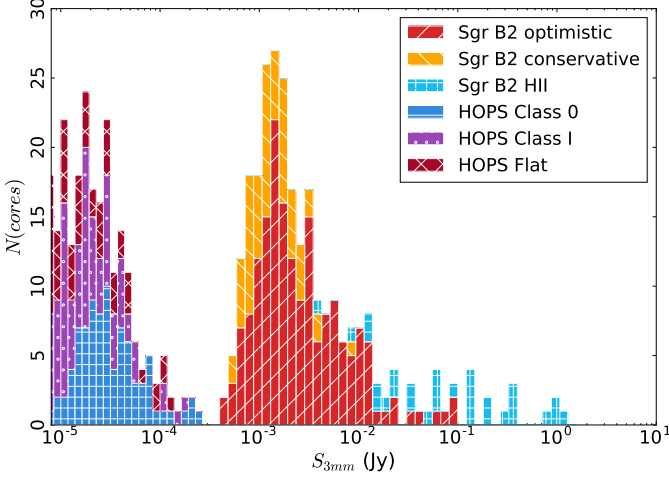


Figure 10. A histogram combining the detected Sgr B2 cores with predicted flux densities for sources at $d = 8.4$ kpc and $\lambda = 3$ mm based on the HOPS (Furlan et al. 2016) survey. The sources are labeled by their infrared (2-20 μm) spectral index: Class 0 and I have positive spectral index and flat spectrum sources have $-0.3 < \alpha_{IR} < 0.3$. The HOPS histogram shows the 870 μm data from that survey scaled to 3 mm assuming $\beta = 1.5$ (see footnote 4). Every HOPS source is well below the detection threshold for our observations.

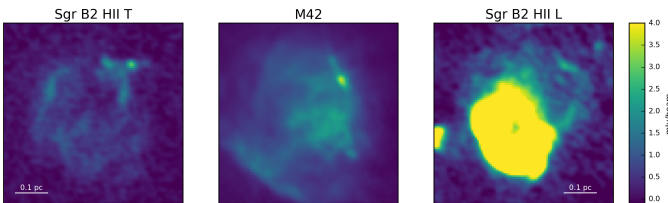


Figure 11. Comparison of two extended H II regions in Sgr B2 (ALMA 3 mm continuum) to the M42 (GBT MUSTANG 3 mm continuum; Dicker et al. 2009) nebula in Orion. The three panels are shown on the same physical and color scale assuming $d_{\text{Orion}} = 415$ pc and $d_{\text{SgrB2}} = 8.4$ kpc and that the ALMA and MUSTANG data have the same continuum bandpass. Sgr B2 H II T is comparable in brightness and extent to M42; Sgr B2 H II L is much brighter and is saturated on the displayed brightness scale. The compact source to the top right of the M42 image is Orion Source I; the images demonstrate that Source I and the entire M42 nebula would be easily detected in our data.

For each subcluster identified in Schmiedeke et al. (2016, see Figure 1), we count the number of H II regions identified in our survey plus those identified in previous works (Gaume et al. 1995; De Pree et al. 1996), and we count the number of protostellar cores not associated with H II regions. The distributions of source flux densities associated with each cluster are shown in Figure 12.

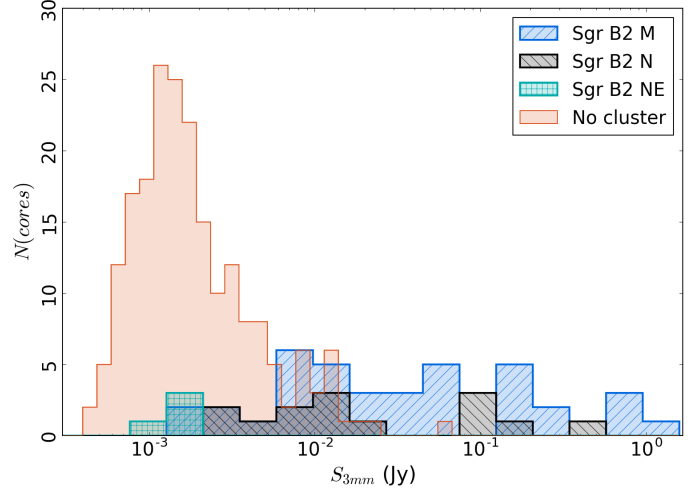


Figure 12. Histograms showing the flux density (the peak intensity converted to flux density assuming the source is unresolved) of the observed sources classified by their cluster association. Unlike Figure 6, the histograms are overlapping, not stacked. The bin widths for the clusters are wider than for the unassociated sources.

We assume each source not associated with an H II region contains or will form a star with mass equal to the average over the range $8-20 M_\odot$ assuming a Kroupa (2001) initial mass function, $\bar{M}(8-20) = 12 M_\odot$ (in this section, we refer to these objects as “cores”). Based on the arguments in Section 3.3.3, we assume each H II region contains a star that is B0 or earlier, and therefore that they have each have a mass equal to the average $\bar{M}(> 20) = 45$. In Table 2, the total counted mass estimate is shown as $M_{\text{count}} = N\bar{M}$.

We also compute the *total* stellar mass (i.e., the extrapolated mass including low-mass stars) using the mass fractions $f(M > 20) = 0.14$ and $f(8 < M < 20) = 0.09$. The total mass is then $M_{\text{tot}} = M_{\text{count}}(M > 20)/f(M > 20) = M_{\text{count}}(8 < M < 20)/f(8 < M < 20)$. The inferred masses computed from H II region counts and from core counts are shown in columns $M_{\text{inferred,H II}}$ and $M_{\text{inferred,cores}}$ respectively. M_{inferred} is the average of these two estimates; it is also what would be obtained if all stars were assumed to be average stars with $M > 8 M_\odot$ (and no upper limit). If our mass range classifications are correct and the mass distribution is governed by a power-law IMF, we expect $M_{\text{inferred,H II}} = M_{\text{inferred,cores}}$. In Sgr B2 N and S, the core-based and H II-region based estimates agree to within a factor of 2, which is about as good as expected from Poisson noise in the counting statistics.

Sgr B2 M contains the largest source sample, and it has a factor of nine discrepancy between the ‘core’ and H II-region based counts. The discrepancy may arise

from the combined effects of source confusion at our $0.5''$ resolution and the increased noise around the extremely bright central region that makes detection of < 2 mJy sources difficult. The majority of pixels within the cluster region have significant detections at 3 mm, but we do not presently have the capability to distinguish between extended dust emission, free-free emission, or a confusion-limited point source population. While it is possible that this discrepancy is driven by observational limitations, we also explore in Section 4.2 the possibility that it is a real physical effect.

We compare our mass estimates to those of Schmiedeke et al. (2016), who inferred stellar masses from H II region counts. The two columns of Table 2 with superscript S show the observed and estimated masses based on H II region counts. For Sgr B2 M and N, our results are similar, as expected since our catalogs are similar. For S and NE, we differ by a large factor, primarily because Schmiedeke et al. (2016) assumed that $M_{min,MYSO}$ and M_{max} were the smallest and largest observed masses in the cluster, while we assumed $M_{min,MYSO} = 8 M_\odot$ and $M_{max} = 200 M_\odot$; i.e., we assumed a spatially invariant IMF.

Finally, we estimate the star formation rate using the above mass estimates. To determine the star formation rate, we need to know the age of the current star forming burst. We use the dynamical model of Kruijssen et al. (2015) to get an age of the Sgr B2 cloud $t = 0.74$ Myr (Longmore et al. 2013). We divide the inferred stellar mass by this age; the results are shown in Table 2. This rate assumes that star formation was initiated at the cloud’s most recent pericenter passage. Our estimated total inferred SFR of the Sgr B2 cloud is $0.038 M_\odot \text{ yr}^{-1}$, between one quarter and one half of the total for the CMZ (Longmore et al. 2013; Barnes et al. 2017). Because of the large number of assumptions above, there is at least a factor-of-two uncertainty on this number.

3.5. An examination of star formation thresholds

Several authors (e.g., Lada et al. 2010; Heiderman et al. 2010) have proposed that star formation can only occur above a certain density or column density threshold⁶. We discuss our measurements of column density thresholds in this section.

3.5.1. Comparison to Lada, Lombardi, and Alves 2010

In this section, we compare the star formation threshold in Sgr B2 to that in local clouds performed by Lada

et al. (2010). They determined that all star formation in local clouds occurs above a column density threshold $M_{thresh} > 116 M_\odot \text{ pc}^{-2}$, or $N_{thresh}(\text{H}_2) > 5.2 \times 10^{21} \text{ cm}^{-2}$ assuming the mean particle mass is 2.8 amu (Kauffmann et al. 2008). We first note, then, that *all pixels* in our column density maps (Section 2.2, Battersby et al, in prep) are above this threshold by *at least* a factor of 10.

However, Sgr B2 is 8.4 kpc away from us in the direction of our Galaxy’s center, meaning there is a potentially enormous amount of material unassociated with the Sgr B2 cloud along the line of sight. This material may have column densities as low as $5 \times 10^{21} \text{ cm}^{-2}$ or as high as $5 \times 10^{22} \text{ cm}^{-2}$, as measured from relatively blank regions in the Herschel column density map (Battersby et al. 2011). The former value corresponds to the background at high latitudes, $b \sim 0.5$, while the latter is approximately the lowest seen within our field of view. Even with the very aggressive foreground value of $5 \times 10^{22} \text{ cm}^{-2}$ subtracted, nearly the whole Sgr B2 cloud exists above the Lada et al. (2010) threshold.

To directly compare our observations to the star formation thresholds reported in Lada et al. (2010), we examined the column density associated with each millimeter continuum source. The Lada et al. (2010) data used a variable resolution for the column density measurements toward their sample, ranging from 0.06–0.35 pc (equivalent to 1.5 to $9.2''$ at a distance of 8.4 kpc). The Herschel data we have available with per-pixel SED fits lack the resolution needed to make a direct comparison to the Lada et al. data set, but the SHARC and SCUBA data have resolution approximately equivalent to that used in the Orion molecular cloud in their survey (see Section 2.2).

Because the higher-resolution images only cover a narrow range of wavelengths and cannot be used to directly measure the dust temperature, we adopt two approaches to approximate the dust temperature. First, we use a two fixed temperatures bracketing the observed range in the Herschel maps ($\sim 20 - 50$ K) to produce column density maps from the SCUBA and SHARC data. Second, we interpolated the Herschel-derived temperature map on to the SHARC and SCUBA grids and used the SHARC and SCUBA intensities with the interpolated temperature to infer the higher-resolution column density.

Figure 13 shows the cumulative distribution function of the column density associated with each identified continuum source; the column density used is the nearest-neighbor pixel to the source in the column density maps. Even using the conservative maximum temperature $T_{dust} = 50$ K (resulting in the minimum col-

⁶Column density is commonly used as a proxy for volume density because of its observational convenience, but volume density is the more meaningful physical parameter for most relevant processes in star formation (e.g., gravity and pressure).

Table 2. Cluster Masses

Name	$N(\text{cores})$	$N(\text{HII})$	M_{count}	M_{inferred}	$M_{\text{inferred,HII}}$	$M_{\text{inferred,cores}}$	M_{count}^s	M_{inf}^s	SFR
			M_{\odot}	M_{\odot}	M_{\odot}	M_{\odot}	M_{\odot}	M_{\odot}	$M_{\odot} \text{ yr}^{-1}$
M	17	47	2300	8800	15000	2300	1295	20700	0.012
N	11	3	270	1200	980	1500	150	2400	0.0017
NE	4	0	48	270	0	540	52	1200	0.00037
S	5	1	110	500	330	680	50	1100	0.00068
Total	240	57	5500	26000	19000	33000	1993	33400	0.035

M_{count} is the mass of directly counted protostars, assuming each millimeter source is $12.0 M_{\odot}$, or $45.5 M_{\odot}$ if it is also an H II region. $M_{\text{inferred,cores}}$ and $M_{\text{inferred,HII}}$ are the inferred total stellar masses assuming the counted objects represent fractions of the total mass 0.09 (cores) and 0.14 (H II regions). M_{inferred} is the average of these two. M_{count}^s and M_{inf}^s are the counted and inferred masses reported in Schmiedeke et al. (2016). The star formation rate is computed using M_{inferred} and an age $t = 0.74$ Myr, which is the time of the last pericenter passage in the Krijssen et al. (2015) model. The *total* column represents the total over the whole observed region. The clusters sum to much less than the *total* because the Deep South region is not included, and it dominates the overall core count.

umn density), all of the sources exist at a column density an order of magnitude higher than the Lada threshold, and they exist above that threshold even if the foreground is assumed to be an extreme $5 \times 10^{22} \text{ cm}^{-2}$. While all of the sources exist above this threshold, not all pixels above this threshold contain protostars or protostellar cores; the threshold is therefore a necessary, but not a sufficient, condition for star formation.

The Lada et al. (2010) sample used Spitzer observations of nearby clouds that were nearly complete to stars at least as small as $0.5 M_{\odot}$. By contrast, as discussed in Section 3.3.4, our survey is sensitive only to stars with $M \gtrsim 8 M_{\odot}$. The apparently higher column threshold either means that there is a genuinely higher threshold for star formation in the CMZ or that there is a higher threshold for high-mass star formation that may still be universal.

3.5.2. Other Thresholds

A theoretical threshold for high-mass star formation, $\Sigma > 1 \text{ g cm}^{-2}$ ($N(\text{H}_2) > 2 \times 10^{23} \text{ cm}^{-2}$) was developed by Krumholz & McKee (2008). Nearly all of the sources we have detected reside above this threshold (independent of the assumed foreground contamination), and we determined our sources are all likely to be massive protostars in Section 3.3.4. However, not all pixels with $\Sigma > 1 \text{ g cm}^{-2}$ are forming high-mass stars (Figure 16). Again, we have inferred the presence of a necessary but not sufficient star formation threshold

However, there is another threshold in our data, $N(\text{H}_2) > 1 \times 10^{24} \text{ cm}^{-2}$, above which the majority of the gas is associated with ongoing high-mass star formation (Figure 16). This threshold suggests that any gas reaching a column density $N(\text{H}_2) > 10^{24} \text{ cm}^{-2}$ over a $\approx 0.5 \text{ pc}$ size scale (the resolution of our column density maps) has more likely than not begun to form

high-mass stars. This column density corresponds to a volume density $n(\text{H}_2) \approx 10^5 \text{ cm}^{-3}$ assuming spherical symmetry.

3.5.3. Comparison to G0.253+0.016

In G0.253+0.016 (The Brick, G0.253), very little star formation has been observed (Longmore et al. 2013; Johnston et al. 2014; Rathborne et al. 2014, 2015) despite most of the cloud existing above the locally measured Lada et al. (2010) column density threshold. The column density distribution function for G0.253 is shown in Figure 14.

The Rathborne et al. (2014) and Rathborne et al. (2015) ALMA 3 mm data are the deepest observations of G0.253 in the millimeter regime to date, with a sensitivity about $4\times$ better than ours, but a beam of $1.7''$ (similar to that shown in Figure 1; compare to Figure 2 in both Rathborne et al papers). Despite the higher sensitivity of their data, they detected only 3 compact continuum sources. Similarly, Kauffmann et al. (2013) detected no compact continuum sources in their SMA and CARMA observations. By contrast, even in our coarse resolution data, which have a worse sensitivity ($\text{RMS} \approx 0.25 \text{ mJy beam}^{-1}$, $10\times$ worse than Rathborne et al), dozens of compact sources are evident. Our better resolution was critical for identifying the hundreds of sources we have identified, but it is nonetheless clear that the star formation activity is much higher in Sgr B2 than G0.253.

Comparing Sgr B2 to G0.253, the majority of the Sgr B2 cloud is at higher column than G0.253. Star formation in Sgr B2 nearly all occurs at a higher column than exists within G0.253 (Figure 14). The dearth of observed cores in G0.253 is therefore easily explained if there is a column density threshold for star formation that is not reached in G0.253. Given that the G0.253

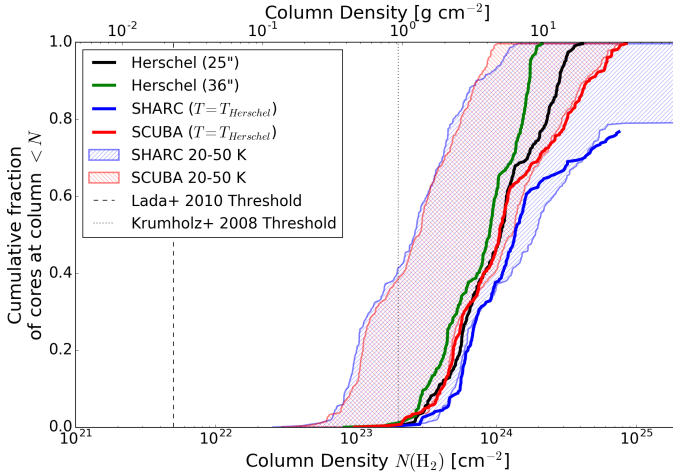


Figure 13. Cumulative distribution functions of the background column density associated with each identified 3 mm continuum source. The column densities are computed from a variety of maps with different resolution and assumed temperature. The Herschel maps use SED-fitted temperatures (Battersby et al. in prep) at 25'' resolution (excluding the 500 μm data point) and 36'' resolution. The SHARC 350 μm and SCUBA 450 μm maps both have higher resolution ($\sim 10''$) but no temperature information; we used an assumed $T_{dust} = 20$ and $T_{dust} = 50$ K to illustrate the range of possible background column densities (hatched red and blue). The thick solid red and blue lines show the SHARC and SCUBA column density images using Herschel temperatures interpolated onto their grids: these curves are closer to the 20 K than the 50 K curve and serve as the best estimate column density maps. The SHARC data fail to go to a cumulative fraction of 1 because the central pixels around Sgr B2 M and N are saturated (the lower temperature assumptions result in optical depths > 1 , which cannot be converted to column densities using the optically thin assumption). The vertical dashed line shows the $N(\text{H}_2) = 5.2 \times 10^{21} \text{ cm}^{-2}$ column density threshold from Lada et al. (2010), and the vertical dotted line shows the $N(\text{H}_2) = 2 \times 10^{23} \text{ cm}^{-2}$ Krumholz & McKee (2008) threshold for high-mass star formation.

observations were deeper than our own, yet still identified almost no forming stars, it appears more likely that there is a lack of star formation rather than simply a lack of high-mass star formation. Nonetheless, robust verification of this hypothesis will require much deeper observations sensitive to low-mass stars in both regions.

3.6. Comparison to Gutermuth et al. 2011

Unlike Lada et al. (2010), who invoke a threshold followed by a linear star formation law relating the gas to the stellar surface density, Gutermuth et al. (2011) concluded that star formation was best represented as power-law relations between the stellar and gas mass surface densities.

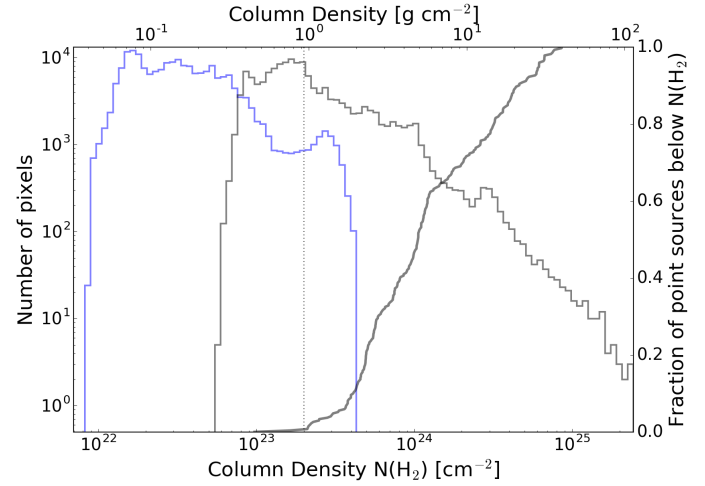


Figure 14. Histograms of the column density of G0.253+0.016 (blue) and Sgr B2 (gray) using the combined SCUBA 450 μm and Herschel 500 μm intensity with the interpolated Herschel dust temperatures. The cumulative distribution of core ‘background’ column densities in Sgr B2 is shown as a thick gray line, showing that the densities at which stars are forming in Sgr B2 are barely reached in G0.253. The vertical dotted line is the Krumholz & McKee (2008) threshold for high-mass star formation at $N(\text{H}_2) = 2 \times 10^{23} \text{ cm}^{-2}$, while the Lada et al. (2010) threshold is below the minimum value plotted here (see Section 3.5).

We adopt the same approach used in Gutermuth et al. (2009) and Gutermuth et al. (2011) to compare gas and stellar mass surface densities. We computed both the star-centric mass surface density using the 11th nearest neighbor density and a gridded surface density. We assume a mean mass per source $\bar{M}(M > 8 M_\odot) = 21.8 M_\odot$, and that each such star represents 23% of the total stellar mass (see Section 3.4), i.e., each 3 mm source is treated as $95 M_\odot$ of stellar mass⁷. The correlation is similar whether we use the Herschel column density directly or the SCUBA or SHARC-based column density maps (see Section 2.2).

There are a few key differences between our data and those of Gutermuth et al. (2011). First, our *minimum* detected column density is $N(\text{H}_2) \approx 10^{23} \text{ cm}^{-2}$, while in their sample, the *maximum* observed was $A_V = 38$, or $N(\text{H}_2) = 3.8 \times 10^{22} \text{ cm}^{-2}$. Even if we subtract our upper-limit foreground estimate $N(\text{H}_2) = 5 \times 10^{22}$ from

⁷In previous sections, we assigned different masses to different source classes, i.e., we assigned higher masses to H II regions than non-H II regions. For consistency with Gutermuth et al. (2011), we assume a constant mass per source here, which may result in a systematic underestimation of the stellar mass surface density at the highest densities (since the H II regions are preferentially concentrated in clusters).

the entire Sgr B2 map, nearly all of the detected sources reside in regions with column densities well above the maximum reached in the local cloud sample. Second, our 3 mm source sample is sensitive to only the youngest sources, either the high-mass equivalent of Class 0/I sources ('hot cores' or HMYSOs), or deeply embedded hypercompact H II regions. The Spitzer sample included both Class I sources, with estimated ages $t \lesssim 0.5$ Myr, and Class II, with ages $0.5 < t < 5$ Myr. Our sample is therefore biased young. If the age estimate for Sgr B2 from the dynamical models (Longmore et al. 2013; Kruijssen et al. 2015) is accurate, there should be about as many Class II sources as Class I, given the standard ages, meaning our total mass estimate may be as much as a factor of 2 underestimated.

Despite the differences in method, the Sgr B2, Mon R2, and Ophiucus clouds have similar instantaneous star formation efficiencies, $\epsilon = M_*/(M_* + M_{\text{gas}})$. Sgr B2 has $\epsilon = 0.016 - 0.018$ (depending on whether the foreground is subtracted), Mon R2 $\epsilon = 0.019$, and Ophiucus $\epsilon = 0.04$.

Figure 15 shows the stellar mass surface density Σ_* plotted against the gas mass surface density Σ_{gas} . Our data show a large scatter and are plausibly compatible with a power-law index in the range 1-2, and therefore overall consistent with the steep slopes ($\alpha \approx 2$) Gutermuth et al. (2011) derived. Figure 15 shows in orange three curves from the Gutermuth et al. (2011) $\alpha = 2$ star formation law, their Equation 7, with $k = 10^{-4} \text{ pc}^2 M_{\odot}^{-1} \text{ Myr}^{-1}$ and $\alpha = 2$, at times $t = 0.01, 0.1$, and 0.74 Myr. Only the youngest curve, with age 0.01 Myr, overlaps with our data. The three red curves, which are essentially lines in this figure, show the $\alpha = 1$ law at the same three ages, and it achieves reasonable agreement with our data for the $t = 0.74$ Myr line.

Figure 15 shows that the extrapolated relation from the low-mass clouds exceeds our observations by at least $50\times$ (Ophiucus) or closer to $10^3\times$ (Mon R2). The star formation law they used is only consistent with our data for times earlier than $t < 0.1$ Myr. This inconsistency is due to the very fast depletion time for this form of star formation law, which rises with gas surface density. Indeed, the $\alpha = 2$ star formation law favored by Gutermuth et al. (2011) is completely implausible for the gas surface density regime we observe, as it implies that gas with an initial surface density of $\Sigma_{\text{gas}} = 10^4 M_{\odot} \text{ pc}^{-2}$ would achieve a star formation efficiency $\epsilon > 1$ in $t < 0.1$ Myr. The discrepancy between our observations and theirs indicates either that there is a systematic tendency to overestimate Σ_* at high Σ_{gas} in the Spitzer observations, which seems unlikely, or that there is a different star formation law in Sgr B2 than in local clouds.

4. DISCUSSION

We have reported the detection of a large number of point sources and inferred that they are most likely all high-mass protostars. These sources universally reside in gas above $N(\text{H}_2) \gtrsim 2 \times 10^{23} \text{ cm}^{-2}$ and are distributed along.

4.1. What drives star formation in the greater Sgr B2 complex?

We have shown that, in addition to the known forming massive clusters, star formation is ongoing in an extended and elongated region to the north and south. Why are the sources aligned? Was star formation in Sgr B2 triggered by a single event?

There are a few different possible triggers that have been considered in the literature: pericenter passage (Longmore et al. 2013; Kruijssen et al. 2015), cloud-cloud collision (Hasegawa et al. 1994; Mehringer & Menten 1997; Sato et al. 2000), and expanding shells driven by massive stars (Martín-Pintado et al. 1999). These scenarios are distinct and apply to different scales. The pericenter passage model assumes that gas is fed into a ~ 100 pc radius non-circular orbit and experiences significant tidal compression at closest approach to the bottom of the gravitational potential. The compression leads to progressively increasing star formation along the CMZ dust ridge. Cloud-cloud collision models assume that independent clouds on different orbits are interacting. The expanding shell model assumes the shells are driven by feedback from a previously formed generation of high-mass stars.

We examine these three possibilities but reach no definitive conclusion about which process is dominant.

4.1.1. Pericenter Triggering

Our observations are reconcilable with a star formation event triggered at pericenter passage. If the entire cloud was stable prior to pericenter passage, at closest approach it would have been simultaneously crushed and stretched by shear (Kruijssen et al. 2015). This event would have driven collapse of the whole cloud, with the densest regions collapsing fastest and possibly forming the clusters we observe today. This model accounts for the relative ages of the extended star formation event and the clustered starbursts (discussed further in Section 4.2), but provides no direct explanation for the morphology of the star formation event.

4.1.2. Cloud-cloud collision

There are no definitive signs of 'cloud-cloud collision' or 'colliding flows' in our line or continuum data, though that is largely because all possible evidence for such

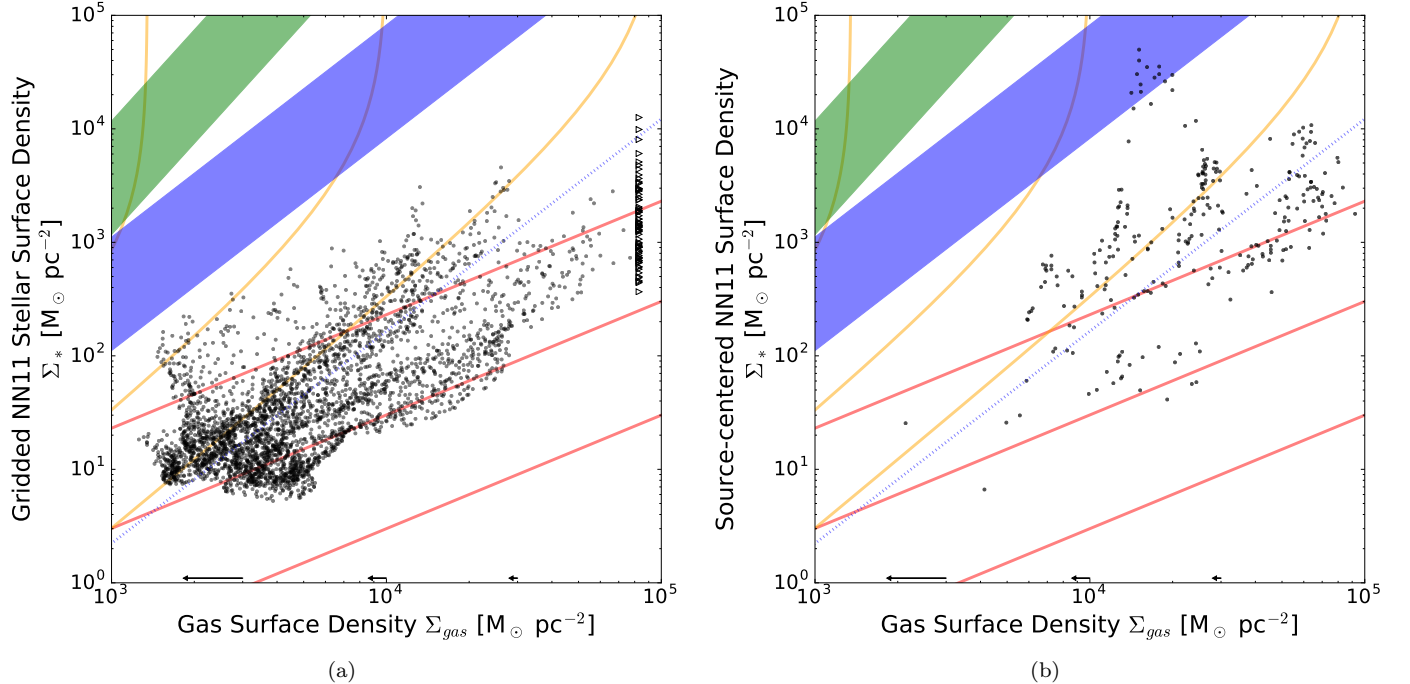


Figure 15. Plots of the protostellar mass surface density vs the gas mass surface density as derived from Herschel SED fitting (Section 2.2). The stellar mass surface densities are computed using the 11th nearest-neighbor distance assuming that each star represents a mass of $95 M_{\odot}$, extrapolated assuming a uniform IMF. (a) shows the densities computed on a 0.25 pc grid, with column density lower limits indicated where the Herschel data are saturated, while (b) shows the protostar-centric surface densities; no lower limits are included in this figure because interpolated mass surface densities are used instead. The shaded regions show the extrapolations of the relations derived by Gutermuth et al. (2011) for Ophiucus (blue) and Mon R2 (green); their data cut off below a mass surface density $\Sigma < 10^3 M_{\odot} \text{ pc}^{-2}$. The blue dotted line shows the Ophiucus relation scaled down by 50× to overlap with our data. The thick orange lines show realizations of the Gutermuth et al. (2011) $\alpha = 2$ star formation law at times 0.01, 0.1, and 0.74 Myr, from bottom to top. Similarly, the thick red lines show realizations of the $\alpha = 1$ star formation law at the same ages. The arrows along the bottom show the effect of subtracting a uniform foreground column density of $N(\text{H}_2) = 5 \times 10^{22} \text{ cm}^{-2}$ ($1100 M_{\odot} \text{ pc}^{-2}$).

flows is highly ambiguous. For example, Haworth et al. (2015) show some of the best cases for cloud-cloud collision using the ‘extended bridge’ in position-velocity between two colliding clouds, but these signatures can be completely hidden when multiple clouds exist along a line of sight or when the clouds’ intrinsic line widths are of the same magnitude as their impact velocity, as in Sgr B2. While multiple line components have been invoked as evidence for cloud-cloud collision (Hasegawa et al. 1994; Corby et al. 2015), such multiple components are also expected in turbulent cloud models. We cannot strictly rule out cloud-cloud collision, but neither can we provide evidence to support it; the kinematic features in our data are compatible with multiple interpretations.

Additionally, most of the notable kinematic features evident in the dense gas images can be attributed to expanding H II regions or otherwise feedback-driven flows (see Section 4.1.3). While interacting independent gas streams are a possible agent affecting Sgr B2, their ef-

fects are not obvious in our core catalog or in the gas data cubes.

We note that some ‘colliding flows’ are expected in almost any collapse scenario. For example, simulations of a cloud passing through Galactic pericenter (Kruijssen et al. in prep.; Dale et al. in prep.) show that some material is ejected during this passage that later collapses back onto the original cloud. It is possible that any apparent colliding flows (e.g., Sato et al. 2000) are a component of this process.

4.1.3. Expanding Shells

There is some evidence of expanding shells (bubbles) in Sgr B2 (de Vicente et al. 1997; Martín-Pintado et al. 1999). We compare the location of the molecular gas traced by HC₃N and the location of the identified 3 mm continuum sources to plausible bubble locations to evaluate whether the bubbles may be responsible for driving the observed star formation.

There is extended ionized emission in Sgr B2 Deep South that appears to be a bubble surrounded by the

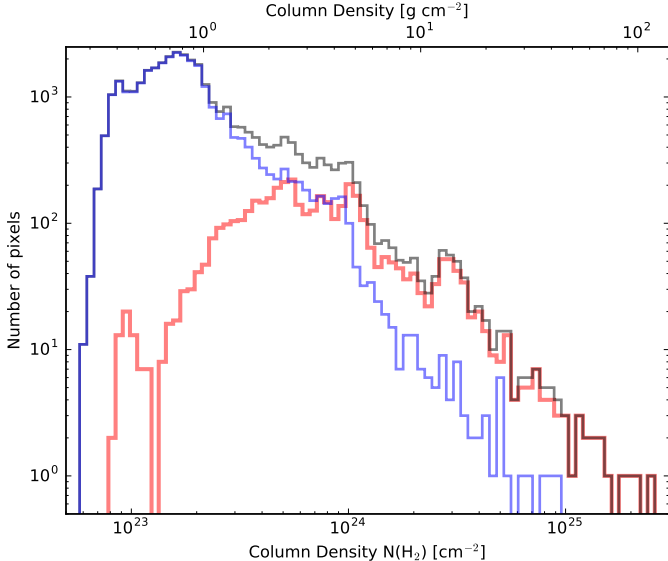


Figure 16. Histograms of the column density measured with the combined SCUBA and Herschel data using the interpolated Herschel temperatures covering only the region observed with ALMA. The black histogram shows the whole observed region, the blue solid line shows the SCUBA pixels that do not contain an ALMA source, and the red thick line shows those pixels that are within one beam FWHM of an ALMA source. While the ALMA sources (high mass protostars and young stars) clearly reside in high-column gas, there is abundant high-column material that shows no signs of ongoing star formation.

millimeter continuum sources. While this region looks like a normal H II region in the 12'' resolution 20 cm VLA data in Figure 8, the 3 mm continuum reveals long filamentary features reminiscent of the Galactic center nonthermal filaments. By analogy, they may be magnetically dominated regions (e.g., LaRosa et al. 2004), but there must be some central source of ionizing radiation or energetic particles. Jones et al. (2011) and Protheroe et al. (2008) reported nonthermal emission from this region, which they called Sgr B2 SC (“Southern Complex”), supporting the idea that it is magnetically dominated. They concluded that the nonthermal emission is not from secondary electrons from cosmic ray interactions, but did not provide an alternative hypothesis. Whatever the driver, it is possible that an expanding bubble of hot gas has compressed the molecular material along the ridge where we observe star formation. Martín-Pintado et al. (1999) identified their bubbles B and F in this region, and suggested that they are driven by Wolf-Rayet stellar winds, which is consistent with both our continuum and line observations. However, the ridge of millimeter sources extends well above the apparent bubble edge, so it is unlikely that the en-

tire DS ridge was driven by a single coherent expanding bubble.

By contrast, the Sgr B2 North bubble, which can be seen as arcs of HC₃N emission in the top-left of Figure 8b, does not contain any ionized emission. It contains fewer total sources than DS, and these sources may trace the edge of an expanding bubble previously noted by de Vicente et al. (1997). However, unlike in DS, the sources are not well-correlated with the HC₃N emission peaks, suggesting that the present bubble expansion is halting rather than driving star formation in Sgr B2 N.

There are other regions within our map that have morphology suggestive of expanding bubbles, but they cannot be definitively identified as bubbles. In Figure 8b, there are several sharp-edged HC₃N features, some of which are rounded and hint at the presence of a central driving source. Figure 17 shows that these ridges are generally associated with high-column density dusty regions. However, none of these regions are associated with identified millimeter sources. If they are expanding shells, these shells are not driving star formation.

While there may be expanding shells that have some effect on where MYSOs are forming, it appears that in general, shells do not provide a sufficient condition to drive star forming bursts.

4.2. The clusters and the extended population

We noted in Section 3.4 that the H II-region-inferred protostellar mass matches the core-inferred protostellar mass to within a factor of 2 in the whole Sgr B2 cloud and the individual clusters excepting Sgr B2 M. In Sgr B2 M, the H II-region inferred mass is $\sim 9\times$ greater than the core-inferred mass. While the lack of faint sources in Sgr B2 M could be an observational limitation, it may be a real effect signifying an evolutionary difference.

Sgr B2 M has more H II regions and is more centrally condensed than any of the other clusters and the distributed star forming population. Assuming that H II regions represent a later stage in protostellar evolution than the dusty protostellar core stage, this difference implies that Sgr B2 M is older than Sgr B2 N and the distributed protostar population. By contrast, along the Sgr B2 DS ridge, there are no H II regions, but there are ~ 100 high-mass protostars, which implies that these protostars began their formation nearly simultaneously. Figure 12 shows this difference graphically; Sgr B2 M has an overall source flux distribution marginally higher than Sgr B2 N but dramatically higher than the unclustered sources.

The large number of probable protostars observed along an elongated ridge allows us to estimate an upper limit on their age. Assuming all of these forming stars

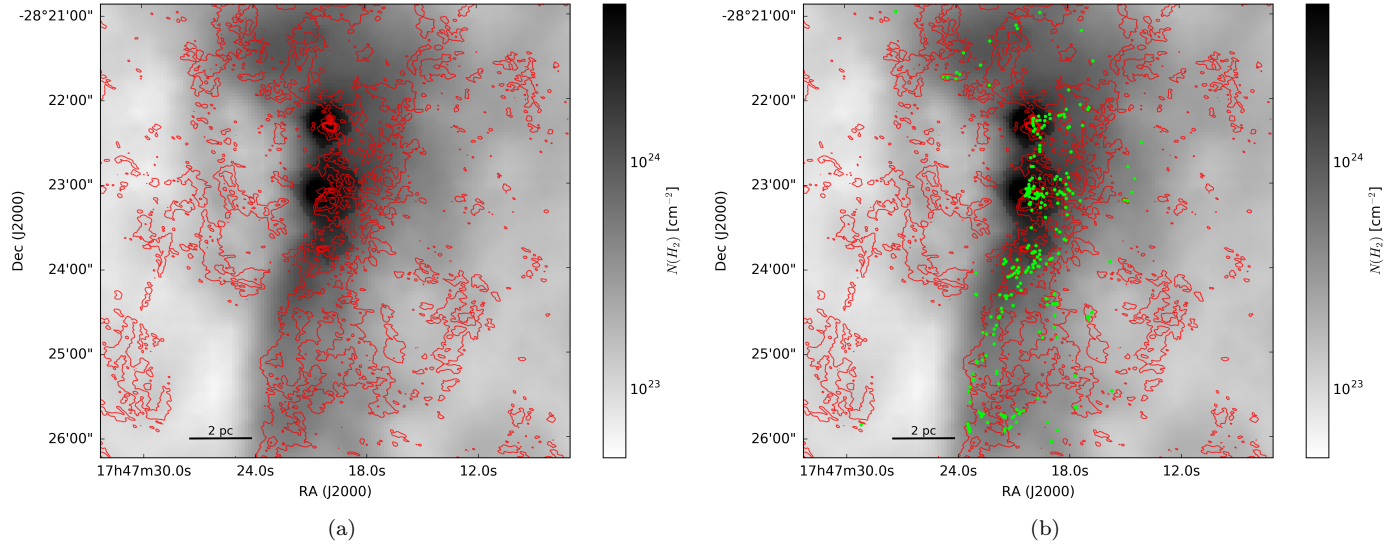


Figure 17. ALMA HC_3N peak intensity contours (red) overlaid on the derived SCUBA column density image using Herschel Hi-Gal interpolated temperatures. The HC_3N was shown in grayscale in Figure 8. Contours are at levels [3,7,11,15,19,23] K. The HC_3N bubble edges can be seen surrounding cavities in the SCUBA column density map on the east side of the main ridge. To the north, the HC_3N also traces bubbles, but these are less evident in this velocity-integrated view. The important feature discussed in Section 4.1 is the differing column density around each of the bubbles. The right figure has the cores overlaid as green dots, showing that the 3 mm sources closely trace the molecular gas, but not all dense molecular gas contains cores or protostars.

are bound to the cloud and/or central clusters, they should approach a spherical distribution within about one crossing time (Efremov & Elmegreen 1998). If we assume the turbulent velocity dispersion is $\sigma_{1D} \approx 10 \text{ km s}^{-1}$ (e.g., Henshaw et al. 2016), and the length of the DS ridge is $L \approx 10 \text{ pc}$, the upper limit on the formation time of the protostars is $L/\sigma_{1D} < 1 \text{ Myr}$. Given the tight alignment of the protostars with the gas ridge (Figures 8 and 17), it is possible to establish a lower upper limit. Most of the sources are within $r < 0.5 \text{ pc}$ of the ‘ridge’, which, assuming they formed in the ridge, suggests an upper age limit $t < r/\sigma_{1D} = 5 \times 10^4 \text{ yr}$. The DS ridge sources appear to be recently formed.

The expanding H II regions observed around Sgr B2 M and N (and assumed to be associated with them) give a lower limit on their ages. The HII regions I, J, A1, and K4 have radii $r \approx 0.1 \text{ pc}$ (Gaume et al. 1995), suggesting their ages are at least $t > 10^5 \text{ yr}$ assuming they are expanding into a density $n \gtrsim 10^5 \text{ cm}^{-3}$ (de Pree et al. 1995; Schmiedeke et al. 2016). The clusters therefore appear to be somewhat older than the ridge sources.

The relative ages of M and the rest of the region (i.e., Sgr B2 M is apparently older) suggest two possibilities for their formation history. If we take the ages at face value, Sgr B2 M must have collapsed first to form stars in an early event, then sometime later the DS ridge began forming stars in a subsequent event. A second pos-

sibility is that the overall collapse of both Sgr B2 M and DS began at the same time, but the Sgr B2 M region was denser and therefore had a shorter collapse time, which is predicted by hierarchical cluster formation models to lead to higher star formation efficiencies (Kruijssen 2012). Our catalog does not allow us to distinguish these possibilities. However, the latter scenario would predict that the cloud should be in a state of global collapse, with the least dense regions collapsing most slowly. This collapse has been suggested to be ongoing in CMZ clouds by Walker et al. (2015, 2016) and may leave detectable kinematic signatures (e.g., self-absorption in moderately optically thick lines) in the dense gas.

Yusef-Zadeh et al. (2009) noted the presence of some Spitzer $4.5 \mu\text{m}$ excess sources and $24 \mu\text{m}$ sources in the southern part of Sgr B2, and from these detections concluded that star formation had proceeded outside-in in the Sgr B2 cloud. Our data have revealed a much larger population of what are most likely younger sources (dust-dominated protostars) in this region, which is inconsistent with the previous interpretation. Instead, it seems that the central clusters are the oldest sites of star formation. The excess of $4.5 \mu\text{m}$ and $24 \mu\text{m}$ sources in DS may be because the cloud’s envelope of opaque material is thinner along those lines-of-sight. We conclude that existing infrared observations of the Sgr B2

cloud lack both the depth and resolution to detect the significant ongoing star formation we report here.

5. CONCLUSIONS

We have reported the detection of 271 3 mm point sources in the extended Sgr B2 cloud and determined that the majority are high-mass protostellar cores. This survey represents the first large population of protostars detected in the Galactic center and represents the largest sample yet reported of high-mass protostars.

The large population of high-mass protostellar cores indicates that an extended region spanning the entire Sgr B2 cloud, not just the well-known clusters N, M, and S, is undergoing a burst of star formation. More than half of the currently forming generation of stars is not associated with any of the clusters but is instead part of the extended burst.

Using Herschel, SCUBA, and SHARC data, we have measured a threshold for high-mass star formation analogous to that done in local clouds by Lada et al. (2010). We find that there are no high-mass protostars in gas below $N(\text{H}_2) < 10^{23} \text{ cm}^{-2}$, at a resolution of $\approx 10'' = 0.4 \text{ pc}$, and half of the detected sources are found above $N(\text{H}_2) > 10^{24} \text{ cm}^{-2}$. These measurements imply either the existence of a higher threshold for high-mass star formation than for low-mass, as predicted by several theories, or a higher threshold for star formation in the Galactic center as compared to local clouds. Deeper observations, recovering the low-mass sources, are required to distinguish these possibilities.

Comparing the protostellar mass surface density to the gas mass surface density revealed a correlation compatible with that observed by Gutermuth et al. (2011). However, there is a large discrepancy in the amplitude....

The large detected population of high-mass protostars implies a much larger population of as-yet undetectable lower-mass protostars. Future ALMA and JWST programs to probe this population would provide the data needed to directly compare star formation thresholds in the most intensely star-forming cloud in our Galaxy to those in nearby clouds.

Software: The software used to make this version of the paper is available from github at https://github.com/keflavich/SgrB2_ALMA_3mm_Mosaic/ with hash 320f4d1(2017-07-20).

Acknowledgements This work is partly supported by a grant from the National Science Foundation (AST-1615311, De Pree). JMDK gratefully acknowledges funding from the German Research Foundation (DFG) in the form of an Emmy Noether Research Group (grant number KR4801/1-1), from the European Research Council (ERC) under the European Union’s Horizon 2020 research and innovation programme via the ERC Starting Grant MUSTANG (grant agreement number 714907), and from Sonderforschungsbereich SFB 881 “The Milky Way System” (subproject P1) of the DFG.

REFERENCES

- Bally, J., Aguirre, J., Battersby, C., et al. 2010, ApJ, 721, 137
- Barnes, A. T., Longmore, S. N., Battersby, C., et al. 2017, MNRAS, 469, 2263
- Battersby, C., Bally, J., Ginsburg, A., et al. 2011, A&A, 535, A128
- Bendo, G. J., Griffin, M. J., Bock, J. J., et al. 2013, MNRAS, 433, 3062
- Bergin, E. A., Langer, W. D., & Goldsmith, P. F. 1995, ApJ, 441, 222
- Bertincourt, B., Lagache, G., Martin, P. G., et al. 2016, A&A, 588, A107
- Beuther, H., Tackenberg, J., Linz, H., et al. 2012, ApJ, 747, 43
- Caswell, J. L., Fuller, G. A., Green, J. A., et al. 2010, MNRAS, 404, 1029
- Chapin, E. L., Berry, D. S., Gibb, A. G., et al. 2013, MNRAS, 430, 2545
- Condon, J. J., & Ransom, S. 2007, Essential Radio Astronomy (NRAO). <http://www.cv.nrao.edu/course/astr534/ERA.shtml>
- Corby, J. F., Jones, P. A., Cunningham, M. R., et al. 2015, MNRAS, 452, 3969
- De Pree, C. G., Gaume, R. A., Goss, W. M., & Claussen, M. J. 1996, ApJ, 464, 788
- de Pree, C. G., Rodriguez, L. F., & Goss, W. M. 1995, RMxAA, 31, 39
- De Pree, C. G., Peters, T., Mac Low, M.-M., et al. 2014, ApJL, 781, L36
- De Pree, C. G., Peters, T., Mac Low, M. M., et al. 2015, ApJ, 815, 123
- de Vicente, P., Martin-Pintado, J., & Wilson, T. L. 1997, A&A, 320, 957
- Di Francesco, J., Johnstone, D., Kirk, H., MacKenzie, T., & Ledwosinska, E. 2008, ApJS, 175, 277

- Dicker, S. R., Mason, B. S., Korngut, P. M., et al. 2009, *ApJ*, 705, 226
- Dowell, C. D., Lis, D. C., Serabyn, E., et al. 1999, in *Astronomical Society of the Pacific Conference Series*, Vol. 186, *The Central Parsecs of the Galaxy*, ed. H. Falcke, A. Cotera, W. J. Duschl, F. Melia, & M. J. Rieke, 453
- Efremov, Y. N., & Elmegreen, B. G. 1998, *MNRAS*, 299, 588
- Furlan, E., Fischer, W. J., Ali, B., et al. 2016, *ApJS*, 224, 5
- Gaume, R. A., Claussen, M. J., de Pree, C. G., Goss, W. M., & Mehringer, D. M. 1995, *ApJ*, 449, 663
- Ginsburg, A., Glenn, J., Rosolowsky, E., et al. 2013, *ApJS*, 208, 14
- Ginsburg, A., Walsh, A., Henkel, C., et al. 2015, *A&A*, 584, L7
- Ginsburg, A., Henkel, C., Ao, Y., et al. 2016, *A&A*, 586, A50
- Green, S., & Chapman, S. 1978, *ApJS*, 37, 169
- Gutermuth, R. A., Megeath, S. T., Myers, P. C., et al. 2009, *ApJS*, 184, 18
- Gutermuth, R. A., Pipher, J. L., Megeath, S. T., et al. 2011, *ApJ*, 739, 84
- Hasegawa, T., Sato, F., Whiteoak, J. B., & Miyawaki, R. 1994, *ApJL*, 429, L77
- Haworth, T. J., Shima, K., Tasker, E. J., et al. 2015, *MNRAS*, 454, 1634
- Heiderman, A., Evans, II, N. J., Allen, L. E., Huard, T., & Heyer, M. 2010, *ApJ*, 723, 1019
- Henshaw, J. D., Longmore, S. N., Kruijssen, J. M. D., et al. 2016, *MNRAS*, 457, 2675
- Higuchi, A. E., Hasegawa, T., Saigo, K., Sanhueza, P., & Chibueze, J. O. 2015, *ApJ*, 815, 106
- Immer, K., Kauffmann, J., Pillai, T., Ginsburg, A., & Menten, K. M. 2016, *A&A*, 595, A94
- Immer, K., Menten, K. M., Schuller, F., & Lis, D. C. 2012, *A&A*, 548, A120
- Johnston, K. G., Beuther, H., Linz, H., et al. 2014, *A&A*, 568, A56
- Jones, D. I., Crocker, R. M., Ott, J., Protheroe, R. J., & Ekers, R. D. 2011, *AJ*, 141, 82
- Jones, P. A., Burton, M. G., Cunningham, M. R., et al. 2012, *MNRAS*, 419, 2961
- Kauffmann, J., Bertoldi, F., Bourke, T. L., Evans, II, N. J., & Lee, C. W. 2008, *A&A*, 487, 993
- Kauffmann, J., Pillai, T., & Zhang, Q. 2013, *ApJL*, 765, L35
- Kauffmann, J., Pillai, T., Zhang, Q., et al. 2016a, ArXiv e-prints, arXiv:1610.03499
- . 2016b, ArXiv e-prints, arXiv:1610.03502
- Kendrew, S., Ginsburg, A., Johnston, K., et al. 2013, *ApJL*, 775, L50
- Kroupa, P. 2001, *MNRAS*, 322, 231
- Kruijssen, J. M. D. 2012, *MNRAS*, 426, 3008
- Kruijssen, J. M. D., Dale, J. E., & Longmore, S. N. 2015, *MNRAS*, 447, 1059
- Kruijssen, J. M. D., & Longmore, S. N. 2013, *MNRAS*, 435, 2598
- Krumholz, M. R., & McKee, C. F. 2008, *Nature*, 451, 1082
- Lada, C. J., Lombardi, M., & Alves, J. F. 2010, *ApJ*, 724, 687
- LaRosa, T. N., Nord, M. E., Lazio, T. J. W., & Kassim, N. E. 2004, *ApJ*, 607, 302
- Lis, D. C., Li, Y., Dowell, C. D., & Menten, K. M. 1999, in *ESA Special Publication*, Vol. 427, *The Universe as Seen by ISO*, ed. P. Cox & M. Kessler, 627
- Longmore, S. N., Kruijssen, J. M. D., Bally, J., et al. 2013, *MNRAS*, 433, L15
- Lu, X., Zhang, Q., Kauffmann, J., et al. 2015, *ApJL*, 814, L18
- Martín-Pintado, J., Gaume, R. A., Rodríguez-Fernández, N., de Vicente, P., & Wilson, T. L. 1999, *ApJ*, 519, 667
- McGrath, E. J., Goss, W. M., & De Pree, C. G. 2004, *ApJS*, 155, 577
- Mehringer, D. M., de Pree, C. G., Gaume, R. A., Goss, W. M., & Claussen, M. J. 1995, *ApJL*, 442, L29
- Mehringer, D. M., & Menten, K. M. 1997, *ApJ*, 474, 346
- Mezger, P. G., & Henderson, A. P. 1967, *ApJ*, 147, 471
- Mills, E. A. C., Butterfield, N., Ludovici, D. A., et al. 2015, *ApJ*, 805, 72
- Molinari, S., Swinyard, B., Bally, J., et al. 2010, *A&A*, 518, L100
- Molinari, S., Bally, J., Noriega-Crespo, A., et al. 2011, *ApJL*, 735, L33
- Molinari, S., Schisano, E., Elia, D., et al. 2016, *A&A*, 591, A149
- Muno, M. P., Bauer, F. E., Baganoff, F. K., et al. 2009, *ApJS*, 181, 110
- Ossenkopf, V., & Henning, T. 1994, *A&A*, 291, 943
- Ossenkopf-Okada, V., Csengeri, T., Schneider, N., Federrath, C., & Klessen, R. S. 2016, *A&A*, 590, A104
- Pierce-Price, D., Richer, J. S., Greaves, J. S., et al. 2000, *ApJL*, 545, L121
- Plambeck, R. L., Bolatto, A. D., Carpenter, J. M., et al. 2013, *ApJ*, 765, 40
- Protheroe, R. J., Ott, J., Ekers, R. D., Jones, D. I., & Crocker, R. M. 2008, *MNRAS*, 390, 683
- Rathborne, J. M., Longmore, S. N., Jackson, J. M., et al. 2014, *ApJ*, 786, 140
- . 2015, *ApJ*, 802, 125

- Rau, U., & Cornwell, T. J. 2011, A&A, 532, A71
- Reid, M. J., Menten, K. M., Zheng, X. W., Brunthaler, A., & Xu, Y. 2009, ApJ, 705, 1548
- Reid, M. J., Menten, K. M., Brunthaler, A., et al. 2014, ApJ, 783, 130
- Robitaille, T. P. 2017, A&A, 600, A11
- Sadavoy, S. I., Stutz, A. M., Schnee, S., et al. 2016, A&A, 588, A30
- Sahai, R., Güsten, R., & Morris, M. R. 2012a, ApJL, 761, L21
- Sahai, R., Morris, M. R., & Claussen, M. J. 2012b, ApJ, 751, 69
- Sanchez-Monge, A., Schilke, P., Schmiedeke, A., et al. 2017, ArXiv e-prints, arXiv:1704.01805
- Sato, F., Hasegawa, T., Whiteoak, J. B., & Miyawaki, R. 2000, ApJ, 535, 857
- Schmiedeke, A., Schilke, P., Möller, T., et al. 2016, A&A, 588, A143
- Schnee, S., Enoch, M., Noriega-Crespo, A., et al. 2010, ApJ, 708, 127
- Shetty, R., Beaumont, C. N., Burton, M. G., Kelly, B. C., & Klessen, R. S. 2012, MNRAS, 425, 720
- Shirley, Y. L., Mason, B. S., Mangum, J. G., et al. 2011, AJ, 141, 39
- Stanimirovic, S. 2002, in Astronomical Society of the Pacific Conference Series, Vol. 278, Single-Dish Radio Astronomy: Techniques and Applications, ed. S. Stanimirovic, D. Altschuler, P. Goldsmith, & C. Salter, 375–396
- Townsley, L. K., Broos, P. S., Garmire, G. P., et al. 2014, ApJS, 213, 1
- Walker, D. L., Longmore, S. N., Bastian, N., et al. 2016, MNRAS, 457, 4536
- . 2015, MNRAS, 449, 715
- Wenger, M., Ochsenbein, F., Egret, D., et al. 2000, A&AS, 143, 9
- Yusef-Zadeh, F., Hewitt, J. W., & Cotton, W. 2004, ApJS, 155, 421
- Yusef-Zadeh, F., Hewitt, J. W., Arendt, R. G., et al. 2009, ApJ, 702, 178
- Zhang, Y., & Tan, J. C. 2015, ApJL, 802, L15

APPENDIX

A. SINGLE DISH COMBINATION

To measure the column density at a resolution similar to Lada et al. (2010), we needed to use ground-based single-dish data with resolution $\sim 10''$. We combined these images with Herschel data, which recover all angular scales, to fill in the missing ‘short spacings’ from the ground-based data.

Specifically, we combine the SHARC 350 μm (Dowell et al. 1999) and SCUBA 450 μm (Pierce-Price et al. 2000; Di Francesco et al. 2008) with Herschel 350 and 500 μm data (Molinari et al. 2016), respectively.

Combining single-dish with ‘interferometer’ data, or data that are otherwise insensitive to large angular scales, is not a trivial process. The standard approach advocated by the ALMA project is to use the ‘feather’ process, in which two images are fourier-transformed, multiplied by a weighting function, added together, and fourier transformed back to image space (see equations in §5.2 of Stanimirovic 2002). This process is subject to substantial uncertainties, particularly in the choice of the weighting function.

Two factors need to be specified for linear combination: the beam size of the ‘single-dish’, or total power, image, and the largest angular scale of the ‘interferometer’ or filtered image. While the beam size is sometimes well-known, for single dishes operating at the top of their usable frequency range (e.g., the CSO at 350 μm or GBT at 3 mm), there are uncertainties in the beam shape and area and there are often substantial sidelobes. In interferometric data, the largest angular scale is well-defined in the originally sampled UV data, but is less well-defined in the final image because different weighting factors change the recovered largest angular scale. For ground-based filtered data, the largest recoverable angular scale is difficult to determine and requires concerted effort (e.g., Ginsburg et al. 2013; Chapin et al. 2013).

To assess the uncertainties in image combination, particularly on the brightness distribution (e.g., Ossenkopf-Okada et al. 2016), we have performed a series of experiments combining the Herschel with the SCUBA data using different weights applied to the SCUBA data. As discussed in Section 2, we empirically determined the scale factor required for the best match between SCUBA and Herschel data was $3\times$, which is shockingly large but justifiable. In the experiment shown in Figure 18, we show the images and resulting histograms when we combine the Herschel data with the SCUBA data scaled by a range of factors from $0.5\times$ to $10\times$. The changes to the high end of the histogram are dramatic, but the middle region containing most of the pixels (and most relevant to the discussion of thresholds in the paper) is hardly affected. Additionally, we show the cumulative distribution function of core background surface brightnesses (as in Figure 13), showing again that only the high end is affected.

B. SELF-CALIBRATION

We demonstrate the impact of self-calibration in this section. The adopted approach used three iterations of phase-only self-calibration followed by two iterations of phase and amplitude self-calibration. Each iteration involved slightly different imaging parameters. The final, deepest clean used a threshold mask on the previous shallower clean. The script used to produce the final images is available at https://github.com/keflavich/SgrB2_ALMA_3mm_Mosaic/blob/320f4d1/script_merge/selfcal_continuum_merge_7m.py. The effects are shown with a cutout centered on the most affected region around Sgr B2 M in Figure 19.

C. PHOTOMETRIC CATALOG

We include the full catalog in digital form (https://github.com/keflavich/SgrB2_ALMA_3mm_Mosaic/blob/master/tables/continuum_photometry_withSIMBAD_andclusters.ipac). Table 3 shows the brightest 35 sources; the rest are included in a digital-only catalog. Sources are labeled based on an arbitrary source number plus any pre-existing catalog name. If a source is associated with a cluster, it has an entry corresponding to that cluster in the `Cluster` column; association is determined by checking whether a source is within a particular distance of the cluster center as defined by Schmiedeke et al. (2016). A source `Classification` column is included, which states whether the source is a strong or weak detection, whether it has an X-ray association, whether it has a maser association, and its SIMBAD classification if it has one. Measurements reported include the peak flux density $S_{\nu,max}$, the corresponding brightness temperature $T_{B,max}$, the integrated flux density within a beam ($0.5''$) radius, the background RMS flux level σ_{bg} as an estimate of the local noise, the spectral index α and the error on that $E(\alpha)$. Mass and column density estimates are given for an assumed temperature $T = 40$ K (M_{40K} and $N(\text{H}_2)_{40K}$). For sources with $T_{B,max} \gtrsim 20$ K, these estimates are unlikely to be useful since the assumed temperature is probably lower than the true temperature.

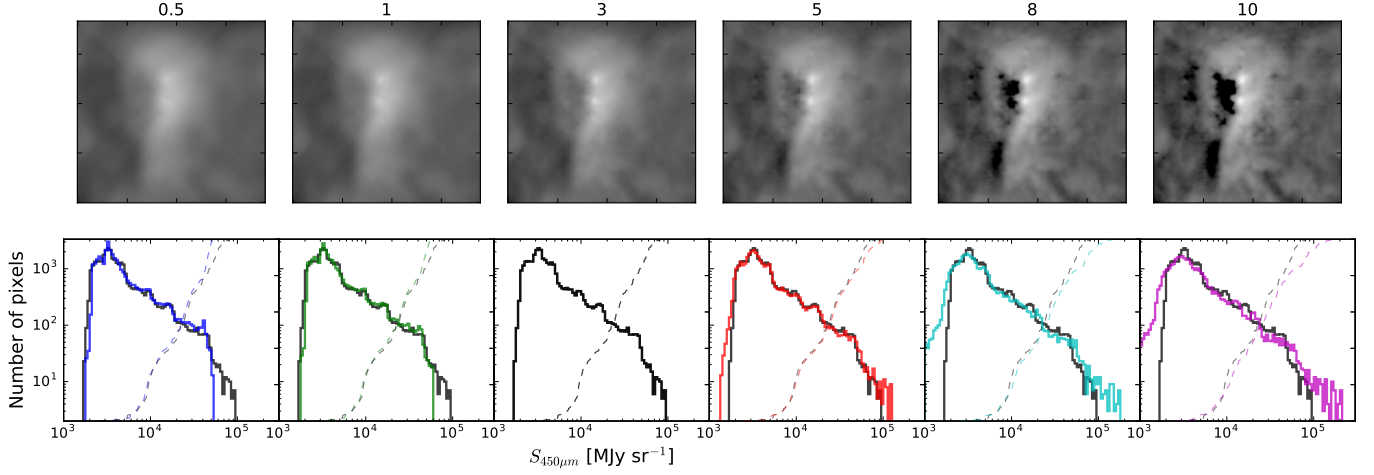


Figure 18. A demonstration of the effects of using different calibration factors when combining the SCUBA data with the Herschel data using the ‘feather’ process. The numbers above each panel show the scale factor applied to the SCUBA data before Fourier-combining it with the Herschel data. The factor of 3 was used in this paper and shows the most reasonable balance between the high-resolution of the SCUBA data and the all-positive Herschel data. In the lower panels, the fiducial scale factor of 3 is shown in black in all panels. The solid lines show histograms of the images displayed in the top panels. The dashed lines show the cumulative distribution of the background surface brightnesses of the point sources in this sample; they are similar to the distributions shown in Figure 13.

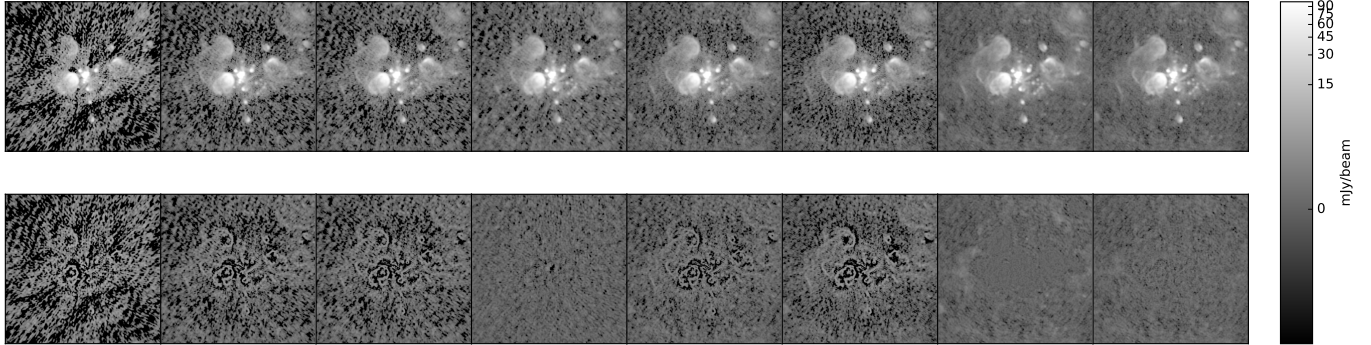


Figure 19. Progression of the self-calibration iterations. The images show, from left to right, the initial image, one, two, and three iterations of phase-only self calibration, two iterations of phase and amplitude self-calibration, a reimaging of the 5th iteration with a deeper 0.1 mJy threshold using a mask at the 2.5 mJy level, and finally, a sixth iteration of phase and amplitude self-cal cleaned to 0.1 mJy over a region thresholded at 1.5 mJy. All imaging was done using two Taylor terms and multiscale clean. The second row shows the corresponding residual images.

For sources with $T_{B,max} > 40$ K, it is not possible to measure a mass assuming $T = 40$ K, so those entries are left empty.

D. ADDITIONAL FIGURES SHOWING HC₃N

The HC₃N line was discussed at various points in the paper. Because the data are extremely rich and complex, we elected not to flood the main paper with figures, but we include some additional figures showing the detailed structure of the lines here.

E. ADDITIONAL FIGURE SHOWING SGR B2 M AND N

We show the Sgr B2 M and N source identifications overlaid on VLA 1.3 cm continuum (De Pree et al. 2014) in Figure 22. This figure highlights the differences between the wavelengths and provides a visual verification that our classification of sources as H II regions is reasonable.

Table 3. Continuum Source IDs and photometry

ID	Cluster	Classification	Coordinates	$S_{\nu,max}$	$T_{B,max}$	$S_{\nu,tot}$	σ_{bg}	α	$E(\alpha)$	M_{40K}	$N(H_2)_{40K}$
				mJy bm $^{-1}$	K	mJy	mJy bm $^{-1}$			M $_{\odot}$	cm $^{-2}$
174 f3	M	S_-W HII	17:47:20.167 -28:23:04.809	1600	860	2400	46	0.89	0.002	-	-
234 f4	M	S_-W HII	17:47:20.214 -28:23:04.379	1100	570	900	23	0.83	0.001	-	-
176 f1	M	S_-W HII	17:47:20.127 -28:23:04.082	920	480	1400	30	1.2	0.006	-	-
236 f10.303	M	S_-W HII	17:47:20.106 -28:23:03.729	890	460	800	19	1.1	0.015	-	-
235 f2	M	S_-W HII	17:47:20.166 -28:23:03.714	820	430	670	33	1.3	0.002	-	-
172 K2	N	S_-W HII	17:47:19.869 -28:22:18.466	370	200	650	49	2.5	0.018	-	-
265 H	S	S_-W HII	17:47:20.461 -28:23:45.404	360	190	580	3.9	0.65	0.019	-	-
175 G	M	S_-W HII	17:47:20.285 -28:23:03.162	340	180	390	5.6	0.68	0.03	-	-
237 G10.44	M	S_-W HII	17:47:20.241 -28:23:03.387	280	140	160	15	0.69	0.006	-	-
178 f10.37	M	SX_-W HII	17:47:20.178 -28:23:06	200	100	270	18	1.5	0.039	-	-
171 K3	N	S_-W HII	17:47:19.895 -28:22:17.221	190	97	280	25	1.4	0.023	-	-
177 B	M	S___ HII	17:47:19.918 -28:23:03.039	150	77	240	3.9	0.47	0.011	-	-
241 f10.30	M	S_-W HII	17:47:20.106 -28:23:03.066	140	73	120	15	1.4	0.05	-	-
179 f10.38	M	S_-W HII	17:47:20.193 -28:23:06.673	130	66	180	9.3	1.6	0.013	-	-
180 E	M	S___ HII	17:47:20.108 -28:23:08.894	130	66	190	4	0.38	0.014	-	-
173 K1	N	S___ HII	17:47:19.78 -28:22:20.743	92	48	150	4.4	0.58	0.034	-	-
170	N	S_-W PartofCloud	17:47:19.895 -28:22:13.621	92	48	160	23	1.7	0.082	-	-
252	N	S_-W denseCore	17:47:19.862 -28:22:13.168	82	43	160	15	1.9	0.078	-	-
225 f10.33b	M	SX_-W denseCore	17:47:20.116 -28:23:06.374	69	36	100	14	1.9	0.21	1200	3.6×10^{26}
264 k4	-	S___ HII	17:47:19.997 -28:22:04.648	65	34	140	3.5	0.57	0.034	1100	2.6×10^{26}
96 Z10.24	-	S_-MW Maser	17:47:20.039 -28:22:41.25	64	33	75	1.5	0.68	0.37	1100	2.5×10^{26}
181 D	M	S_-M_- HII	17:47:20.051 -28:23:12.91	59	31	94	1.3	0.64	0.088	990	2×10^{26}
240 f10.44b	M	S_-W HII	17:47:20.252 -28:23:06.463	57	30	51	11	1.8	0.015	960	1.8×10^{26}
233 f10.27b	M	S_-W HII	17:47:20.077 -28:23:05.383	50	26	78	18	2.3	0.18	840	1.4×10^{26}
239	M	S_-W denseCore	17:47:20.242 -28:23:07.222	45	24	46	8.6	2.3	0.091	760	1.1×10^{26}
244 C	M	S___ -	17:47:19.981 -28:23:18.437	35	19	67	0.49	0.47	0.081	600	7.8×10^{25}
242 f10.318	M	S_-W HII	17:47:20.129 -28:23:02.247	32	17	63	8.5	2.2	0.099	540	6.8×10^{25}
92 I10.52	M	S___ HII	17:47:20.324 -28:23:08.2	32	17	45	5.3	0.63	0.061	530	6.6×10^{25}
245 A2	-	S___ HII	17:47:19.562 -28:22:55.916	25	13	32	2.1	0.54	0.025	410	4.8×10^{25}
109	N	S_-W -	17:47:19.901 -28:22:15.54	24	13	41	13	3.6	0.3	410	4.7×10^{25}
87 B9.99	M	S___ HII	17:47:19.798 -28:23:06.942	23	12	37	1.9	0.89	0.042	390	4.4×10^{25}
88	M	S_-W -	17:47:19.617 -28:23:08.26	23	12	34	2.9	3.1	0.18	380	4.3×10^{25}
151 B10.06	M	S_-M_- HII	17:47:19.86 -28:23:01.5	21	11	31	1.3	0.19	0.79	350	3.8×10^{25}
98	-	S_-M_- Maser	17:47:19.53 -28:22:32.55	18	9.5	29	0.36	3.2	1.1	300	3.3×10^{25}

The Classification column consists of three letter codes as described in Section 3.3. In column 1, S indicates a strong source, W indicates weak or low-confidence source. In column 2, an X indicates a match with the [Muno et al. \(2009\)](#) Chandra X-ray source catalog, while an underscore indicates there was no match. In column 3, M indicates a match with the, [Caswell et al. \(2010\)](#) Methanol Multibeam Survey CH₃OH maser catalog, while an underscore indicates there was no match. Finally, we include the SIMBAD ([Wenger et al. 2000](#)) source object type classification if one was found.

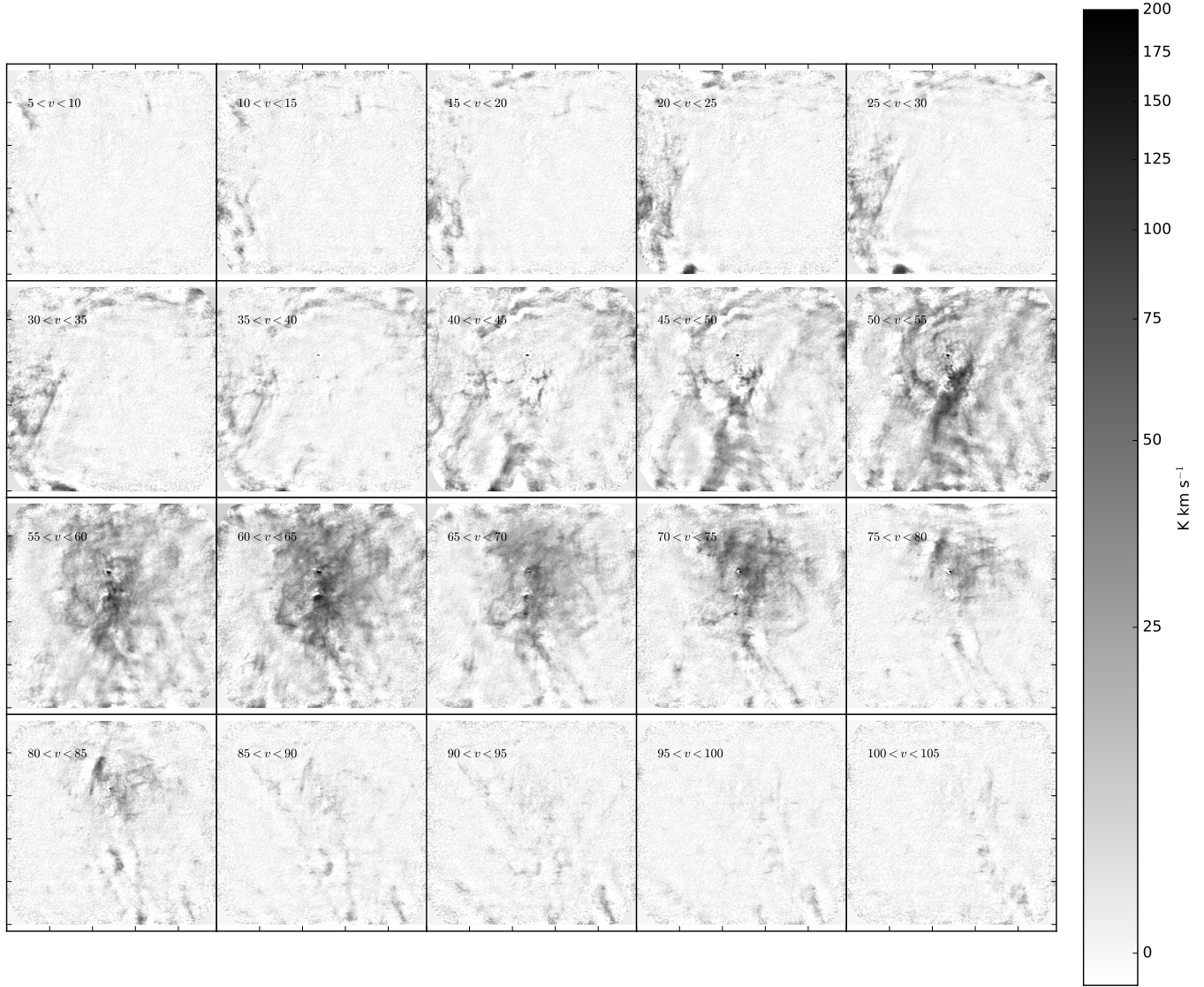


Figure 20. Channel maps of the HC_3N $J=10-9$ line. Each panel shows the integrated intensity over a 5 km s^{-1} velocity range as indicated on the figures. The data shown here are 12m+7m images made excluding the long-baseline data sets to emphasize large angular scales combined with total power data by feathering the images.

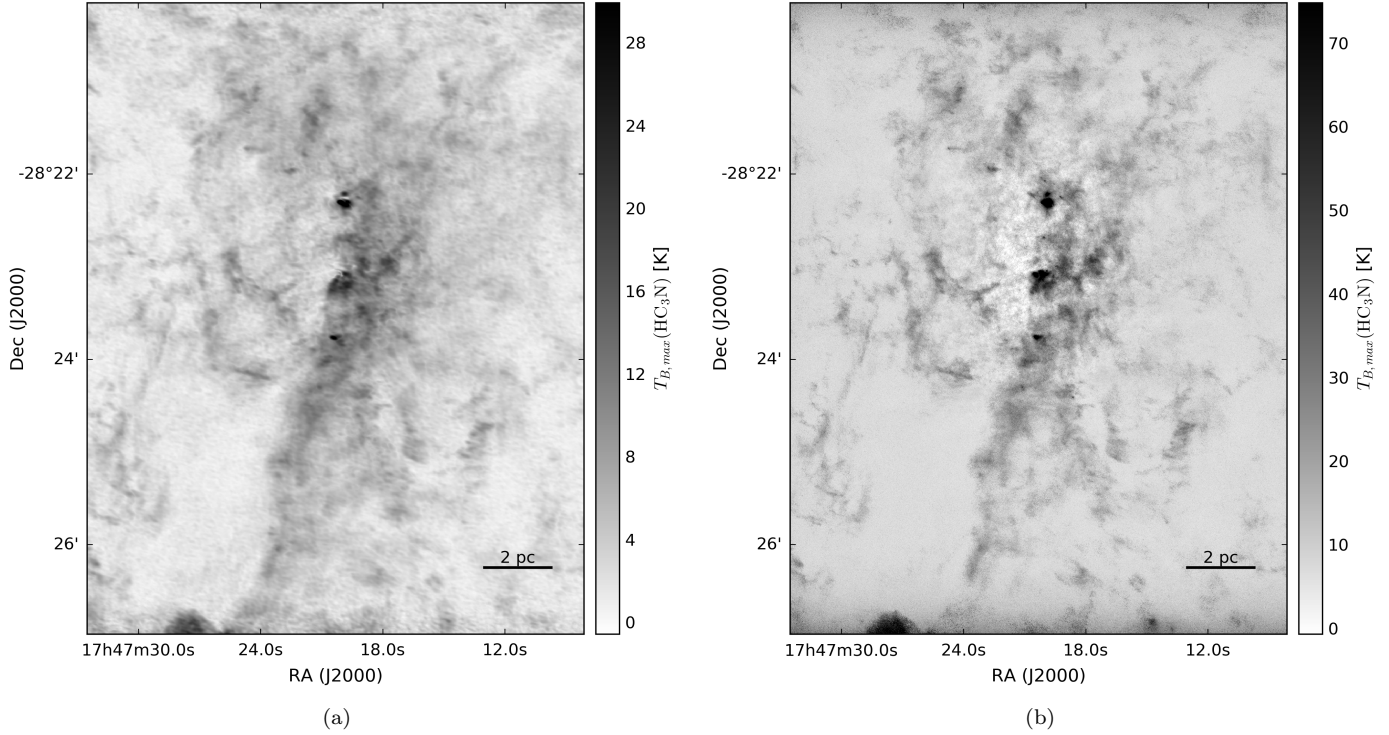


Figure 21. Peak intensity maps of HC₃N J=10-9. The left image shows the 12m short-baseline data combined with 7m and total power data; by excluding the long-baseline data, the large angular scales are emphasized. The right image shows the robust 0.5-weighted 12m+7m data combined with total power data; it reaches a substantially higher peak intensity in the compact regions, but the lower-intensity diffuse emission is relatively hidden. In the right image, the negative bowls seen near Sgr B2 M and N in this peak-intensity image indicate that intermediate size scales were not well-recovered. The bright feature on the bottom-left of both images may be an imaging artifact.

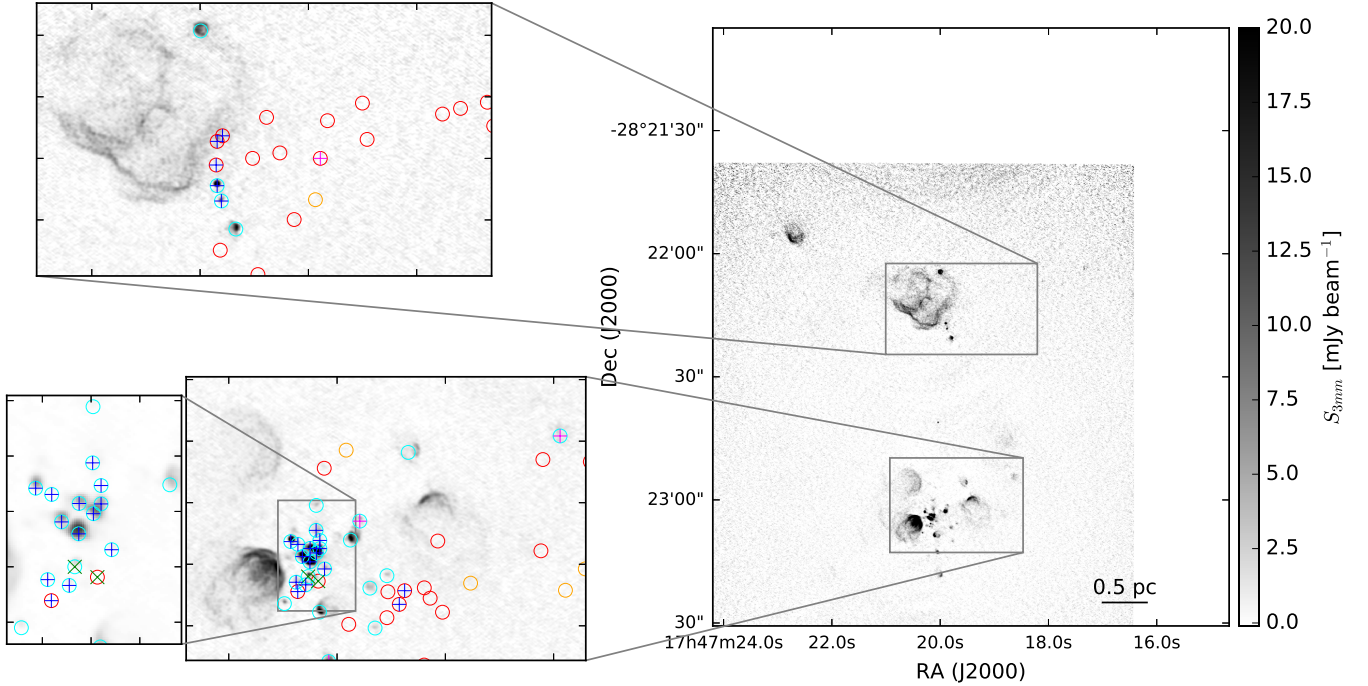


Figure 22. A close-up of Sgr B2 M and N similar to Figure 3, but with VLA 1.3 cm continuum (De Pree et al. 2014) in the background instead of the ALMA 3 mm continuum. Many of the features that appear in the 3 mm image do not appear in the 1.3 cm image and are likely to be from dust emission, but the poorer sensitivity of the 1.3 cm data also suggests that some of these features are simply free-free emission undetected at 1.3 cm.